Universidad de La Laguna

AN OPTICAL STUDY OF GARNET CRYSTALS DOPED WITH NEODYMIUM IONS UNDER AMBIENT AND EXTREME CONDITIONS OF TEMPERATURE AND PRESSURE

Author: Alfredo Casasnovas Melián

Academic tutors: Dr. Víctor Lavín della Ventura

Dr. Ulises Ruymán Rodríguez Mendoza

Academic Year 2018-2019

Table of contents

1. Introduction

Justification and objectives

In Physics, knowledge about how matter is constituted is essential to understand how our world works. So, it is interesting to build theories to predict the behavior of different phenomena. This comprehension can be reached by different techniques of characterization. Spectroscopy techniques are based in the interaction of radiation with matter and provide a powerful tool for this purpose. Optical spectroscopy covers the ultraviolet (UV), visible (VIS), and near-infrared (NIR) ranges of the electromagnetic spectrum, being in general a non-invasive technique that allows to conserve the samples. Especially, some spectroscopic techniques will be used to characterize different garnet crystals, all of them doped with trivalent neodymium ions, Nd^{3+}, whose stoichiometric general formula is given as: $RE_{3(1-x)}Nd_{3x}Ga_yAl_zO_{12}$, where RE^{3+} is trivalent yttrium, Y^{3+}, with factors $x = 0.01$, $y = 0$ or 5 and $z = 0$ or 3, according to the sample. Concretely, the lattice samples that will be analyzed are: $Y_3Al_5O_{12}$, $Y_3Ga_2Al_3O_{12}$ and $Y_3Ga_5O_{12}$, abbreviated as Nd:YAG, Nd:YAGG and Nd:YGG, respectively.

All these garnets, especially Nd:YAG, are the most used garnet to make laser devices of solid state, which are used for the industry, [Strohmaiera et al. 2007; Walsh et al. 1999], medicine [Latina et al. 1998], remote sensing [Kavaya et al. 1989; Löhring et al. 2011], or telecommunication applications [Österberg 1986], as well as for laboratory research, being interesting to characterize these materials, comparing or studying new ways to manufacture them with a good quality and at low cost. Besides to this, it is useful subjecting the materials under extreme thermodynamic conditions such temperature or pressure, because with these methods permit to study structural alterations, unknown phase changes, or even corroborate theoretical quantum phenomena never demonstrated before, as well as simulate conditions found in the center of planets, where garnet structures are abundant, or other stellar bodies [Chiarotti et al 1997].

Theoretical background

In this chapter will be introduced the microscopic model and some crystallographic information, as well as some theoretical considerations for calculations made in the results chapter.

Electronic structure of rare earths

It is well known that electronic disposition in atoms follows two important principles: the Pauli's Exclusion Principle, where two electrons cannot be in the same orbital with the same quantum numbers; and the Hund's Multiplicity Rule, saying that a level is filled according to the total angular moment number. So, for a good number of atoms, concretely for 1st, 2nd and from 13th to 18th group, the electrons are placed in an orderly way and in increasing order of energy, filling progressively their orbitals. Once is filled, the next atom will occupy another. Last electrons compose the unfilled valence shell with different number of electrons depending on the group.

However, this discussion is not the same for the rare earth atoms (*RE*). The reason dwells for the latter, that the valence shell is filled, having an internal orbital unfilled, labelled as $4f^N$. This shell, which will be completed increasing the atomic number for the *RE* ($N = 1, \dots, 14$), is shielded by $5d^1 6s^2$ shells. Because of the object of this study are the crystal garnets which have been doped with Nd^{3+}, which it has lost 3 electrons from his most external shells, the electronic configuration is:

$$Nd^{3+} = [Xe]4f^3$$

where the $4f$ shell is partially populated with three electrons. So, thank to this losing, Nd^{3+} ions will have interesting properties as paramagnetism, and the ability to be optically active (having light absorption and emission) in the optical range. The characterization, from a mathematical point of view, of the energy level scheme for this ion needs to analyze the system as the addition of different terms in the total Hamiltonian. The first term to introduce is the polyelectronic Hamiltonian as shows the reference [Cohen-Tannoudji et al. 1977], characterized by *Z* electrons in a much more massive immobile nucleus at the coordinate origin, and neglecting relativistic effects, expressed as:

$$H_0 = \sum_{i=1}^{Z} \frac{\mathbf{P}_i^2}{2m_e} - \sum_{i=1}^{Z} \frac{Ze^2}{R_i} + \sum_{j>i}^{Z} \frac{e^2}{\left|\mathbf{R}_i - \mathbf{R}_j\right|} \tag{1}$$

where the first term is the kinetic energy, beavering as a free particle; the second term is due to the Coulomb interactions between the nucleus and each electron; and the last contribution is for inter-electronic interaction between the electrons that are in the unfilled $4f$-electrons. Besides to the first non-relativistic approximation, it is necessary to introduce the spin-orbit effect, given by the fine-structure theory:

$$H_{so} = \sum_{i=1}^{N} \xi(r_i) s_i l_i \tag{2}$$

and the crystal-field Hamiltonian that parametrizes the Coulomb interactions between the 4f-electrons and the valence electrons of the ligands in the solid:

$$H_{cf} = \sum_{l,m} A_{l,m} \sum_{i} r_{i,l} Y_l^m(\theta_i, \phi_i) \tag{3}$$

where the $A_{l,m}$ are the crystal-field parameters. So, $H = H_0 + H_{so} + H_{cf}$ is the complete Hamiltonian. These last parameters explain the energy splitting into $^{2S+1}L_J$ multiplet, breaking the degeneracy of the free-ions Hamiltonian. In the next chapters will be discussed the transition bands obtained in the absorption and emission spectra.

Crystallographic information

The translational symmetry of the lattices is a body centered cubic (bcc), showing Morrison that the unit cell parameter is the same in the three directions, i.e. $a = 12.00930$ Å [Morrison and Leavitt 1982]. The space group is *Ia-3d*, No. 230, and the local point symmetry given by the Nd^{3+} and its 8 first neighbors is D_{2d}, although it is usually studied as a cubic structure with an orthorhombic distortion [Lavín et al. 2015]. In Table 1 is shown the crystallographic information according to reference [Morrison and Leavitt 1982]. Shown in Fig. 1, the lattice is composed by octahedrons and tetrahedrons, which leave gaps for the yttrium which has a dodecahedral environment.

Table 1. Crystallographic data for the YAG lattice.

Ion	Position	Symmetry	x	y	z
Y	24(c)	D_2	0	1/4	1/8
Al_1	16(a)	C_{3i}	0	0	0
Al_2	24(d)	S_4	3/8	0	1/4
O	96(h)	C_1	x	y	z

Analysis of spectral lines of absorption and emission spectra

A quantitative treatment for RE^{3+} bands is possible to do considering the Lorentz's model, that is a semi-classical model where the particles of the material behave as some driven harmonic oscillators. If the light falls upon the material with certain energies that coincide with a characteristic energy of an oscillator, a resonance phenomenon will occur and a peak will be seen in an absorption spectrum, as well as in the emission one.
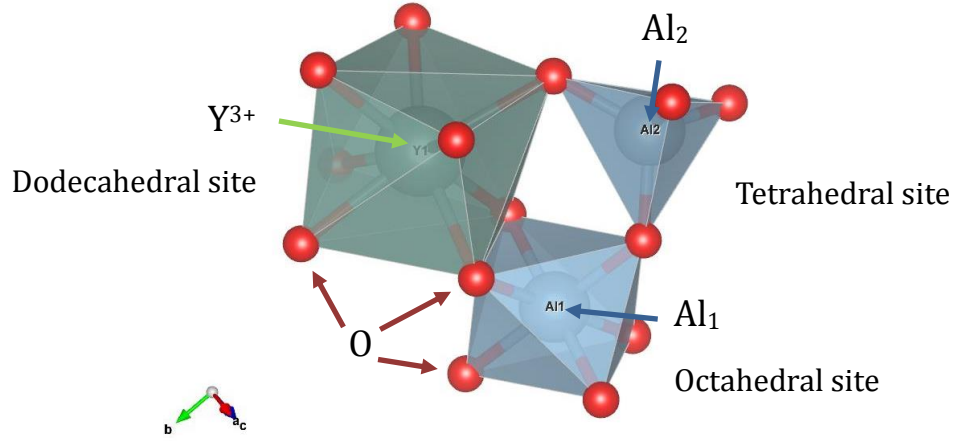
Figure 1. Crystalline unit cell.

Theoretical treatment of absorption and emission spectra of lanthanide ions

According to Carnall [Carnall 1978], it can be related an experimental band envelope called f_{exp}, with a theoretical model based on how radiation can be absorbed in a sample. According to this notation, f is referred to the oscillator strength, and the sub-index comes from the experimental transition. Each oscillator strength given earlier is described by an electric-dipole induced mechanism, $f_{E.D.}$, and by a magnetic dipole contribution too, $f_{M.D.}$. Also, higher multipole mechanisms are neglected, so the relation can be written as follows:

$$f_{exp} = f_{E.D.} + f_{M.D.} \tag{4}$$

In 1962, B.R. Judd [Judd 1962] and G.S. Ofelt [Ofelt 1962] demonstrated that the electric-dipole mechanism, $f_{E.D.}$ can be expressed like a sum over the intensities of the crystal-field components, in a given state. And in truth, this sum can be made over the lowest crystal-field levels of the ground and excited states. The theoretical oscillator strength from the ground state J to the excited state J' can be described as [Carnall 1978; Rodríguez-Mendoza et al. 2011]:

$$f(aJ; bJ') = \frac{8\pi^2 mc}{3h(2J+1)\bar{\lambda}e^2 n^2}\{\chi_{E.D.}\, f_{E.D.}(aJ; bJ') + \chi_{M.D.}\, f_{M.D.}(aJ; bJ')\} \tag{5}$$

where the factors for the electric and magnetic dipole transitions are:

$$\chi_{E.D.} = \frac{n(n^2+2)^2}{9} \qquad\qquad \chi_{M.D.} = n^3 \tag{6}$$

being m the electron mass, in g; c is the speed of the light, in cm/s; h the Plank's constant, in erg·s; J is the total angular momenta quantum number, and used in absorption spectra, is

referred to the corresponding to the ground state for the RE^{3+} doping ion, dimensionless; $\bar{\lambda}$, the average wavelength band (calculated as the gravity center), in cm; the electron charge e, in $dyn^{1/2} \cdot cm$; and n is the refractive index for the material, varying according to the wavelength. The electric-dipole oscillator strength is given by [Judd 1962; Ofelt 1962]:

$$f_{E.D.}(aJ; bJ') = e^2 \sum_{t=2,4,6} \Omega_t \left| \langle f^N[\alpha SL]J | U^{(t)} | f^N[\alpha'S'L']J' \rangle \right|^2 \tag{7}$$

in bra-kets notation: the α symbol is referred at all quantum numbers necessary to characterize the f^N state with a combination of S spin quantum number, L the angular momentum number, and J the total quantum number; the Ω_t, $t = (2, 4, 6)$, are the Judd-Ofelt intensity parameters. The matrix elements $\left| \langle f^N[\alpha SL]J | U^{(t)} | f^N[\alpha'S'L']J' \rangle \right|^2$ will be identified as $\left| \langle U^{(t)} \rangle \right|^2$ are the doubled-reduced matrix elements of unitary tensors of rank t, independent of the host. They can be described as [Judd 1962; Ofelt 1962]:

$$\begin{aligned} \langle [f^N \alpha SL]J | U^{(t)} | [f^N \alpha'S'L']J' \rangle = \\ = \delta_{S,S''}(-1)^{S+L'+J+t}[(2J+1)(2J'+1)]^{1/2} \begin{Bmatrix} J & J' & t \\ L' & L & S \end{Bmatrix} \langle f^N \alpha SL | U^{(t)} | f^N \alpha' S' L' \rangle \end{aligned} \tag{8}$$

having the Kronecker's delta over the initial and the final spin numbers, and a combination of the different quantum numbers and the t rank from the unitary tensor. It is notorious a basis change, from the SL to the intermediate-coupling basis. The reason of this change is that the spin-orbit Hamiltonian, Eq. (2), cannot be treated as a perturbation, thus is required to work in basis with the same contributions for L and S. For magnetic-dipole oscillator strengths, they can be expressed as [Rodríguez-Mendoza et al. 2011]:

$$f_{M.D.}(aJ; bJ') = \left(\frac{eh}{4mc} \right)^2 \left| \langle f^N[\alpha SL]J | \vec{L} + 2\vec{S} | f^N[\alpha'S'L']J' \rangle \right|^2 \tag{9}$$

where $\vec{L}$ is the angular momentum and $\vec{S}$ is the spin operators. These matrix elements can be given changing from the SL to the intermediate-coupling basis too. This magnitude contributes to the calculations only when a transition conserves the quantum numbers $\Delta L = 0$, $\Delta S = 0$ and $\Delta J = 0, \pm 1$ [Walsh 2006]. These matrix elements are tabulated, and they can be used when is required. On the other hand, the theoretical oscillator strengths, Eq. (5), could be compared with the experimental ones defined as:

$$f_{exp} = \frac{mc^2}{\pi e^2 \bar{\lambda}^2 N} \frac{2.303}{l} \int OD(\lambda) d\lambda \tag{10}$$

6

where N is the doping ion concentration, in atoms/cm^{-3}; l is the sample's thickness, in cm; and the $OD(\lambda)$ is the optical density, a function that is related with the ratio of the lamp to the sensor intensities, once is trespassed the light in the sample.

According to the Beer-Lambert's law, and considering that the first surface which is fallen upon the light does not show any reflective phenomena, it can be written as:

$$I(\lambda) = I_0 e^{-\alpha(\lambda)l} \tag{11}$$

with $I(\lambda)$ and I_0 (depending on λ too) the transmitted and the source light intensities, respectively. Also, it has been introduced the absorption coefficient $\alpha(\lambda)$. So, solving for the absorption coefficient:

$$\log\left(\frac{I_0}{I}\right) = \log e \, \alpha(\lambda)l \tag{12}$$

This is a relation for the optical density and the absorption coefficient, so, Eq. (10) is written as:

$$f_{exp} = \frac{mc^2}{\pi e^2 \bar{\lambda}^2 N} \int \alpha(\lambda)d\lambda \tag{13}$$

where the absorption coefficient α is given in cm^{-1} units, and the wavelength $\bar{\lambda}$ is given in cm, so the oscillator strength force is a dimensionless magnitude.

Having all these ideas in front, if terms in Eqs. (10) and (13) are compared, and considering only electric-dipole mechanisms for transition bands, it is defined the measured line oscillator strength as:

$$S_m = \frac{3hc(2J+1)}{8\pi^3 e^2 \bar{\lambda} N} \frac{9n}{(n^2+2)^2} \int \alpha(\lambda)d\lambda \tag{14}$$

with the same constants introduced earlier, and the line oscillator strength S_m in cm^2 units. In addition, this expression can be equaled to the Ω_t parameters seen in Eq. (7) as:

$$S_{cal} = \sum_{t=2,4,6} \Omega_t \left|\langle U^{(t)}\rangle\right|^2 \tag{15}$$

So, it is necessary to solve this equation system, formed by N line oscillator strengths (from the transition bands number), and three Judd-Ofelt parameters. However, it has to be imposed that the difference between the measured and calculated line oscillator strength forces must be minimum. It is required to obtain the first derivative and equal to zero to obtain the parameters that minimizes the difference. This procedure will generate a N linear

equation system, where the measured line oscillator strengths and the matrix elements of the unitary tensors of rank t are involved, summarizing all the procedure as a matrix system equation, as follows:

$$\mathbf{\Omega} = \left(A^\dagger A\right)^{-1} A^\dagger S_m \tag{16}$$

where $\mathbf{\Omega}$ is the Judd-Ofelt parameters matrix; A is the matrix given by the unitary tensors for all transitions; and S_m is the matrix where they are the measured line oscillator strength forces. About matrix dimension, A is an $N \times 3$ matrix, S_m is an $N \times 1$ matrix, so $\mathbf{\Omega}$ it is obvious that will have a 3×1 dimension. Once obtained these parameters, it is possible to obtain the theoretical (calculated) line oscillator strengths S_{cal}, again as a matrixial calculation:

$$S_{cal} = A\mathbf{\Omega} \tag{17}$$

Finally, it can be defined the quality factor X [Kaminskii and Li 1974] as follows:

$$X = \frac{\Omega_4}{\Omega_6} \tag{18}$$

related with the spontaneous probability $A(aJ; bJ')$. The quality of the fitting can be expressed by the minimum root-mean-square deviation:

$$\Delta S_{rms} = \left(\frac{\sum(S_{cal} - S_m)^2}{q - p}\right)^{1/2} \tag{19}$$

where it must be needed to sum over the differences between the calculated and experimental line strength oscillator forces squared, and dividing by the difference of the number of analyzed line group, q, in this case the number of areas considered, combined or not; and p, the number of intensity parameters, in this case, three.

Relaxation of excited states

Once the sample is pumped to one of the absorption bands, the next step to analyze the de-excitation mechanisms of the excited states of RE^{3+} ions embedded in a crystalline lattice. Radiative relaxation processes were formulated firstly by J. Axe [Axe 1963], wanting to express how radiative processes could be related with Judd-Ofelt theory, considering an emission of real photons absorbed by optically active ions. Introducing the spontaneous

transition probability $A(aJ; bJ')$ given by references [Rodríguez-Mendoza et al. 2011; Carnall 1978]:

$$A(aJ; bJ') = A_{E.D.} + A_{M.D.} =$$
$$= \frac{64\pi^4}{3h\bar{\lambda}^3(2J+1)n}\{\chi_{E.D.}S_{E.D.}(aJ; bJ') + \chi_{M.D.}S_{M.D.}(aJ; bJ')\} \quad (20)$$

where $A_{E.D.}$ and $A_{M.D.}$ are the spontaneous transition probabilities induced by electric and magnetic dipole effects, respectively, related with the Einstein's coefficients. In the case seen earlier, if a transition does not obey the selection rules for the quantum numbers, then it should consider the electric-dipole case, meanwhile the magnetic-dipole mechanisms are neglected. If not, it will be summed too. So, it results as:

$$A(aJ; bJ') = A_{E.D.} = \frac{64e^2\pi^4}{3h\bar{\lambda}^3(2J+1)}\frac{n(n^2+2)^2}{9}\sum_{t=2,4,6}\Omega_t|\langle U^{(t)}\rangle|^2 \quad (21)$$

From that parameter, the radiative lifetime τ_{rad} of an excited state is obtained as:

$$\tau_{rad} = \left\{\sum_{bJ'}A(aJ; bJ')\right\}^{-1} \quad (22)$$

summing over the manifold possible de-excitation states, with the same total momentum number from the excited level, and the branching ratio β is given by:

$$\beta = \frac{A(aJ; bJ')}{\sum_{bJ'}A(aJ; bJ')} = \tau_{rad}A(aJ; bJ') \quad (23)$$

The first publications about non-radiative processes W_{NR} were presented in the 1960's too. In these processes, the ions which are embedded in the lattice do not de-excite by photon emission, only by a combination of multiphonon W_{MP} and energy transfer processes W_{ET}, being a coulombic type interaction. Thus, the total de-excitation probability can be written as the contribution of the radiative processes $A(aJ; bJ')$ which they have just seen, and the non-radiative processes W_{NR} as:

$$\frac{1}{\tau_{exp}} = A(aJ; bJ') + W_{NR} = \frac{1}{\tau_{rad}} + W_{MP} + W_{ET} \quad (24)$$

being τ_{exp} the experimental lifetime measured in the laboratory; meanwhile τ_{rad} is the radiative lifetime calculated based on Eq. (22). The experimental lifetime values are obtained integrating the experimental curves as:

$$\langle \tau \rangle \equiv \tau_{exp} = \frac{\int It\ \mathrm{dt}}{\int_{-\infty}^{\infty} I\ \mathrm{dt}} \tag{25}$$

with $\int It\ \mathrm{dt}$ is the integrated intensity at time, while $\int_{-\infty}^{\infty} I\ \mathrm{dt}$ is the normalized intensity. This lifetime can be compared with τ_{rad} introducing the luminescence quantum efficiency η_q, that represents the number of photons emitted as a fraction of the photons absorbed, being able to calculate as [Yumashev et al. 2017]:

$$\eta_q = \frac{\tau_{exp}}{\tau_{rad}} \tag{26}$$

Also, multiphonon probability W_{MP} is expressed as [Rodríguez-Mendoza et al. 2011]:

$$W_{MP} = W_0[1 - \exp(hv/k_BT)]^{\Delta E/hv} \tag{27}$$

where W_0 is the rate at 0 K; ΔE is the energy gap involved; and v the relevant energy.

Another non-radiative mechanism is produced when optically active ions are sufficiently close among them, being useful to introduce the concept of energy transfer among ions. When an excited ion is de-excited, called as donor ion, a fraction of its energy is transferred to neighbor ions, called as acceptors, being excited. Increasing the acceptor ion concentration can produce a shortening in the τ_{exp}, even it could produce a donor's luminescence quenching.

It is important to define the non-radiative donor-acceptor energy transfer probability $W_{DA}(R)$ that, based on considering an electric dipole-dipole interaction, can be calculated as [Lavín 2000]:

$$W_{DA}(R)_{E.D.-E.D.}^{(6)} = \frac{C_{DA}^{(6)}}{R^6} \tag{28}$$

having the donor-acceptor transfer parameter $C_{DA}^{(6)}$ as the electric-dipole contribution and R is the inter-ionic donor-acceptor distance. This probability appears from a multipolar expansion, because it can be considered that donor and acceptor ions are separated enough [Lavín 2000].

One way to know this inter-ionic distance for donor and acceptor is using the Inokuti-Hirayama model [Lavín et al. 2015; Dowell 1990], which fits the fluorescence decay intensity with the time $I(t)$ after a pulse of radiation:

$$I(t) = I_0 \exp\left[-\left(\frac{t}{\tau_0}\right) - Qt^{3/S}\right] \tag{29}$$

being I_0 the intensity at time $t = 0$; τ_0 is the intrinsic lifetime of the engaged donor level; the S factor ($S = 6, 8, 10$) is related with the dominant de-excitation mechanism between Nd^{3+} ions, being 6 the electric dipole-dipole contribution; the Q factor is the energy transfer parameter, defined in turn as:

$$Q = \frac{4\pi}{3}\Gamma\left(1 - \frac{3}{S}\right)N_0 R_0^3 \tag{30}$$

dimensionless, $\Gamma\left(1 - \frac{3}{S}\right)$ is the gamma function; N_0 is the concentration of acceptor, equal to the concentration of donors; and R_0 is the critical transfer distance defined as the donor-acceptor separation. The parameter $C_{DA}^{(6)}$ can be related to the Q factor as [Lavín 2000]:

$$C_{DA}^{(6)} = \left(\frac{Q}{4\pi \cdot \Gamma(1/2)N_0}\right)^2 \tag{31}$$

Luminescence Intensity Ratio technique (LIR)

This technique permits to study the behavior of thermalized levels with temperature, comparing the changes in the intensities of their emissions. Considering that all states have got the same probability transition, it can be expected that the proportionality of the population between these two states follows the Boltzmann distribution, so this ratio is the quotient of the most energetic peak to the lowest [Lavín 2000]:

$$R = \frac{I_{31}}{I_{21}} = Ce^{-\beta\Delta E} \tag{32}$$

where I_{31} and I_{21} are the intensities that were integrated from the thermalized multiplets, dimensionless; $\Delta E = E_{31} - E_{21}$ is the average energy gap between these peaks, in energy units, cm^{-1}; $\beta = 1/k_B T$ is the thermodynamic beta; k_B is Boltzmann's constant, in cm^{-1}/K, and T is the system temperature, in K. The C constant is a mixing of other factors:

$$C = \frac{c_{31}(\nu)}{c_{21}(\nu)}\frac{A_{31}g_3 h\nu_{31}}{A_{21}g_1 h\nu_{21}} \tag{33}$$

being $c_{ij}(\nu), ij = 31, 21$ the energy response of the instrument response, related with the sensor behavior, that can be omitted because of all our emission spectra have been

calibrated; A_{ij} are the spontaneous radiative emission coefficients from the excited level i to ground state j, only estimated using the Judd-Ofelt Theory; g_i are the degeneration numbers associates to each state (2J+1) possibilities of each multiplet; and $h\nu_{ij}$ is the photon energy involved between the excited i and the ground states j. The ratio equation is independent of the experimental setup, being compared some spectra obtained with the same correction factors.

It can be presented the absolute sensitivity S_a as the rate of change of the luminescence intensity ratio with temperature and the luminescence ratio, whose units are the inverse of the temperature, in K^{-1}:

$$S_a = \left|\frac{dR}{dT}\right| = \frac{\Delta E}{k_B T^2} R \tag{34}$$

This parameter is interesting when there comparing different materials, like glasses, crystals or ceramics, among them. Also, it is introduced the relative sensitivity S_r denoting that a higher energy gap allows a larger sensitivity. The expression is given by:

$$S_r = 100 \cdot \frac{1}{R}\left|\frac{dR}{dT}\right| = 100 \frac{\Delta E}{k_B T^2} \tag{35}$$

where this relation has got a limited validity because the best values are obtained when ΔE are larger, but it happens when the thermalized level has got a low population, having an important losing of signal-noise ratio and, in consequence, a considerable data uncertainty.

2. Methodology

In this chapter it will be introduced the instruments used, as well as the techniques and set-ups prepared to carry out the experiments. This will be divided in three sections. First of all, it will be mentioned about ambient conditions, and later, it will be introduced all paces followed about the temperature and pressure studies.

Crystal growth and sample preparation

The samples were synthetized by Akira Yoshikawa Group at the Institute of Materials Research, IMR, located in the prefecture of Sendai (Japan), with a stoichiometric mixture of Nd_2O_3, Y_2O_3, $\beta - Ga_2O_3$ and $\alpha - Al_2O_3$ powders. Nominally, Y^{3+} sites were substituted by

Nd^{3+} in 1 % concentration, for all samples. Single crystals were grown by micropulling down method μ-PD using radio-frequencies [Kamada et al. 2011].

Previously to do any measurement, all samples were cut and polished, reducing the thickness of the samples, and removing imperfections. At first, the faces were polished carefully with some sandpapers of different grains, firstly with a 600 and later with 1200 grain number and lubricated with water. A useful technique to polish is doing "eights", to equalize all sides. Later, it was used diamond dust of 1 μm grain, in a soft surface, doing the same movements. Pieces were polished until at the surfaces were not visible any imperfection, having an optical grade and once done that, a mineral cutting machine to reduce the length. Later the new face was polished equally.

Ambient conditions: preparation and instrumentation

In relation to the laboratory conditions, measurements depend on weather conditions, as atmospheric pressure, humidity or temperature. However, in the case of temperature, it has been controlled with a constant value around $20 \pm 2\ °C$, an important factor how will be seen later. All set-up configurations were optimized previously to collect best signal results.

Absorption

The device used was an **Agilent Cary 5000 UV-Vis-NIR** spectrophotometer. Several absorption spectra were taken different configurations to obtain a proper resolution-signal-time relation. The final spectra were obtained from 250 nm for Nd:YAG, and 290 nm for Nd:YAGG to 910 nm, with a 0.1 nm spectral resolution and an integration time of 1 s for both of them. For Nd:YGG, the setup parameters were similar, although the spectral resolution was 0.5 nm, and the measure range started at 300 nm. In special the 800-900 nm interval was taken with a function that it obtained the highest signal-noise ratio.

Luminescence

Two spectrometers were used. One of them is a **TRIAX 320** equipped with a NIR extended PMT photomultiplier, used to acquire the spectrum from 850 nm to 930 nm, opening the slit around 50 μm with a spectral resolution of 0.1 nm and an integration time of 500 ms. using a grating with 600 groves/mm and a 1500 blaze. About high voltage power supply unit, it was used a **Hamamatsu HV** unit, which is supplying electricity to the

spectrometer, it was set in 750 V. As the excitation source was used a **Spectra Physics 3900S** tunable laser, tuned in $^4H_{5/2}$, $^2H_{9/2}$ band at 805 nm, with 46 mW power.

The other emission device is a detector with a CCD sensor, an **ANDOR SR-303i-A** to acquire from 830 nm to 1450 nm. The instrument was configured using the grating with 1200 lines/mm; a blaze of 1000 nm and a slit of 60 μm. It was used to do the rest of the spectrum, from 930 nm to 1120 nm, to all samples, letting two seconds of measuring time to Nd:YAG, 4 s to Nd:YAGG and 15 s to Nd:YGG.

Lifetime

To obtain the lifetimes of the garnets, it has been used an Optical Parametric Oscillator OPO, that is a pulsed excitation source, been able to produce laser flashes with a range of work of the order of nanoseconds. The OPO used was an **EKSPLA NT-342/3/UVE**. The signal was processed with TRIAX 320, a **LeCroy WaveSurfer 424** oscilloscope and a **Hamamatsu NIR PMT Module Controller**. It was used as a trigger a **Hamamatsu S5971** Silicon diode and a 1 $k\Omega$ and 1 W nominal power resistor to convert current signal to voltage signal, and an **Oriel Model 70710** ADC.

Extreme conditions: preparation and instrumentation

Temperature

Low temperature experiments were made using a *He* close cycled cryostat connected to a vacuum pump to cool down until 12 K. In addition to this, a thermocouple is in contact with the sample with copper grease, which permits to conduct the heat and obtain the thermodynamic equilibrium. ANDOR spectrometer was used to obtain the luminescence spectra.

Pressure

It is concerned to use a device that it permits achieve extreme pressures, like a Diamond Anvil Cell (DAC), this is one of the hardest materials in nature, and almost transparent in the optical range. It consists in two diamonds confronted, faced and finished each one in an hexadecagon plane surface of $0.18 \pm 0.03 \text{ mm}^2$, subjecting samples contained between them until 50 GPa of pressure applying a little bit of force, thanks to that tiny area. However, if it is applied pressure touching both diamond surfaces, they will break because they have the same hardness. For this reason it must be introduced a gasket, a metal

piece (in this case tungsten carbide, W_3C) whose thickness was reduced from 220 μm to 50 μm applying pressure with the same diamond heads, using a **Heindenhain ND221B** digital Gauge to control cavity, named as *culot*, whose center is pierced using an **Almax EasyLab**, an electroablation drill which configuration setup is analogic. The machine will do a 100 ± 2 μm radius hole, although sometimes it pierces a minor radius. Once the gasket is ready, it is necessary to charge the pressure cell. Introduced and fixed the gasket (and correctly aligned closing the cell), it is essential to introduce a ruby and a shard of sample inside the hole made in the gasket, it can be seen in Fig. 2.

A ruby sphere ($Cr^{3+}: Al_2O_3$) is used as pressure sensor to identify what pressure is being applied in the cavity, using the expression $p(\text{GPa}) = 2.74\left(\lambda_{R_1} - \lambda_{R_1}^0\right)$, with $\lambda_{R_1}^0$ is referred to the wavelength of the peak R_1 at P=0 GPa [Recio et al. 2016]. Exciting the sphere in 532 nm, two well differentiate peaks are obtained around at 700 nm. Before closing the cell, the cavity is filled with hydrostatic transmitting liquid with a great optical transmittance for having hydrostatic conditions in the cavity. The solution consists in methanol, ethanol and water ($CH_3OH - C_2H_5OH - H_2O$) in $16:3:1$ proportion.
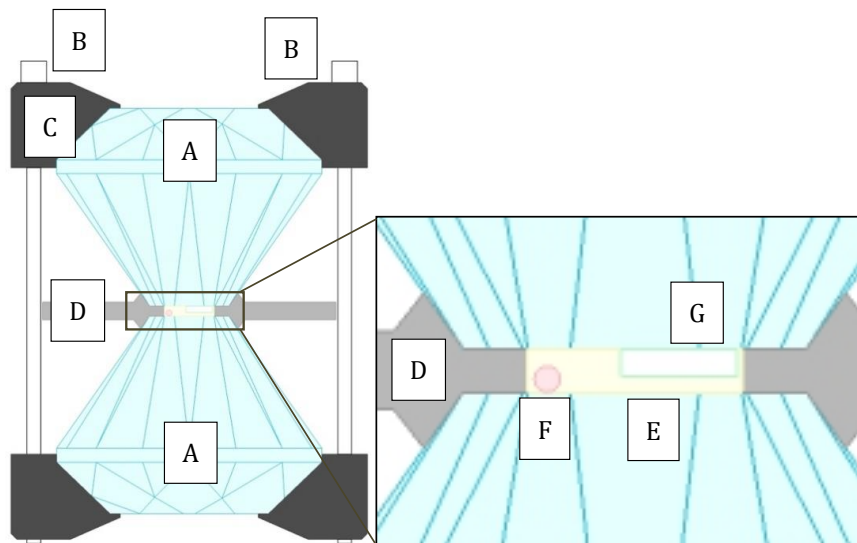

Figure 2. Left: diamond anvil cell scheme. Right: sample preparation. Legend: A: Diamond anvils. B: Nuts. C: Support. D: Gasket. E: Culot with hydrostatic liquid and sample. F: Ruby sphere. G: Sample to analyze.

Finally, all the pressure measurements were made using a **RENISHAW inVia Raman Microscope**, that combines a 532 nm or a 785 nm tuneable lasers, and two respective gratings, referred to the first laser with 1800 lines/mm and 1200 lines/mm the other. The slit was opened in 60.2 μm, and the integration and analyses ranges differed according to the signal obtained.

3. Results

The experimental results are presented and discussed for the three samples at ambient conditions, as well as for the extreme conditions, of temperature and pressure.

Ambient conditions

Absorption measurements

In Fig. 3 are shown the absorption spectra of the undoped hosts, and they allow analyzing the fundamental absorption edges, whose values are shown in Table. They are similar among them, corresponding the lowest gap energy with Nd:YGG sample, meanwhile the highest is for Nd:YAG, being 1.2 times larger. This value indicates the transition from the conduction to the valence band of the host, where electronic transitions due to the Nd^{3+} are within the band gap. Another important parameter is the refractive index, Eqs. (36) and (37), inset in Fig. 3, being taken from reference [Morrison and Leavitt 1982]:

$$n_{YAG}^2(\lambda) = 1 + 2.2779\lambda^2/(\lambda^2 - 0.01142) \tag{36}$$

where λ must be given in μm, using the Sellmeier formula. For YGG had to be approximated with the Cauchy's equation, where λ must be given in μm too:

$$n_{YGG}(\lambda) = 1.905 + 0.013/\lambda^2 \tag{37}$$

For YAGG host could not be found any bibliographic reference about the refractive index expression, and since it was not possible to be studied, it was considered to take the arithmetic average of the refractive indexes of YGG and YAG samples as an approximation, Nd:YAGG is a composition of Al and Ga, being general mixing of Nd:YAG and Nd:YGG, and maybe even this parameter is closer to Nd:YGG, watching the fundamental absorption edge. This parameter must be known because is related to the Judd-Ofelt theory, seeing Eqs. (5), (6), (14), (20) and (21). The ion dopant concentration was obtained balancing the chemical equation, whose results are presented in Table 2.

Table 2. Energy gap values and ion concentrations at 1 mol % for the hosts given.

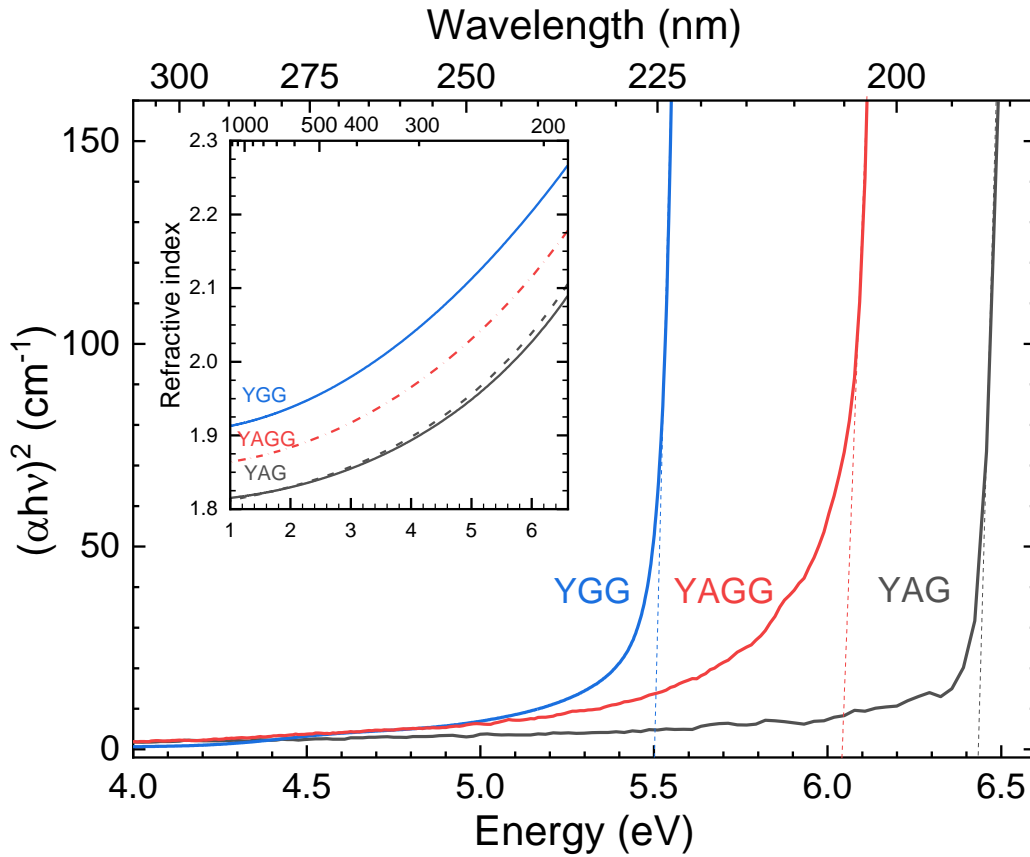| Host	Energy gap (eV)	$N_{Nd^{3+}}$ (at./cm^3)
YAG	6.43	$1.4\cdot10^{20}$
YAGG	6.04	$8.8\cdot10^{19}$
YGG	5.50	$8.3\cdot10^{19}$

Figure 3. Absorption spectra for the samples at ambient conditions, shown the fundamental absorption edges. Inside, the known refractive indexes are given in reference [Morrison and Leavitt 1982].

In Figs. 4 to 6 are presented the absorption spectra for the samples doped at 1% with Nd^{3+}, from whom the garnet undoped absorption contribution has been subtracted. The Stark splitting is produced by the crystal-field of the environment, corresponding to the Nd^{3+} electronic transitions, where the ions absorb the radiation from its ground state $^4I_{9/2}$ to upper levels produced by electric-dipole mechanisms. In general, it is observed sharpened profiles of these peaks in all the samples, usually in RE^{3+} spectra in crystals, confirming that there are Nd^{3+} ions embedded in the crystalline network lattices. In order to identify the manifold bands, data from the literature were used [Morrison and Leavitt 1982; Dong et al. 2005; Krupke 1971; Carnall et al. 1968], including the Dieke's diagram in reference [Carnall 1978], finding a few discrepancies among them. The three samples have got similar profiles, but the absorption coefficients vary, having the highest values for Nd:YAGG and the lowest one for Nd:YGG. For Nd:YAG, the most intense peak is located at 586 nm, for the transition $^4G_{5/2}$, $^2G_{7/2}$, but for Nd:YAGG and Nd:YGG corresponds with the $^4F_{5/2}$, $^2H_{9/2}$ transitions. Seeing the manifold barycenters in Table 3, some of them present slight differences, realizing that the influence of the lattice in the Nd^{3+} ions environment, besides affecting the values of α.
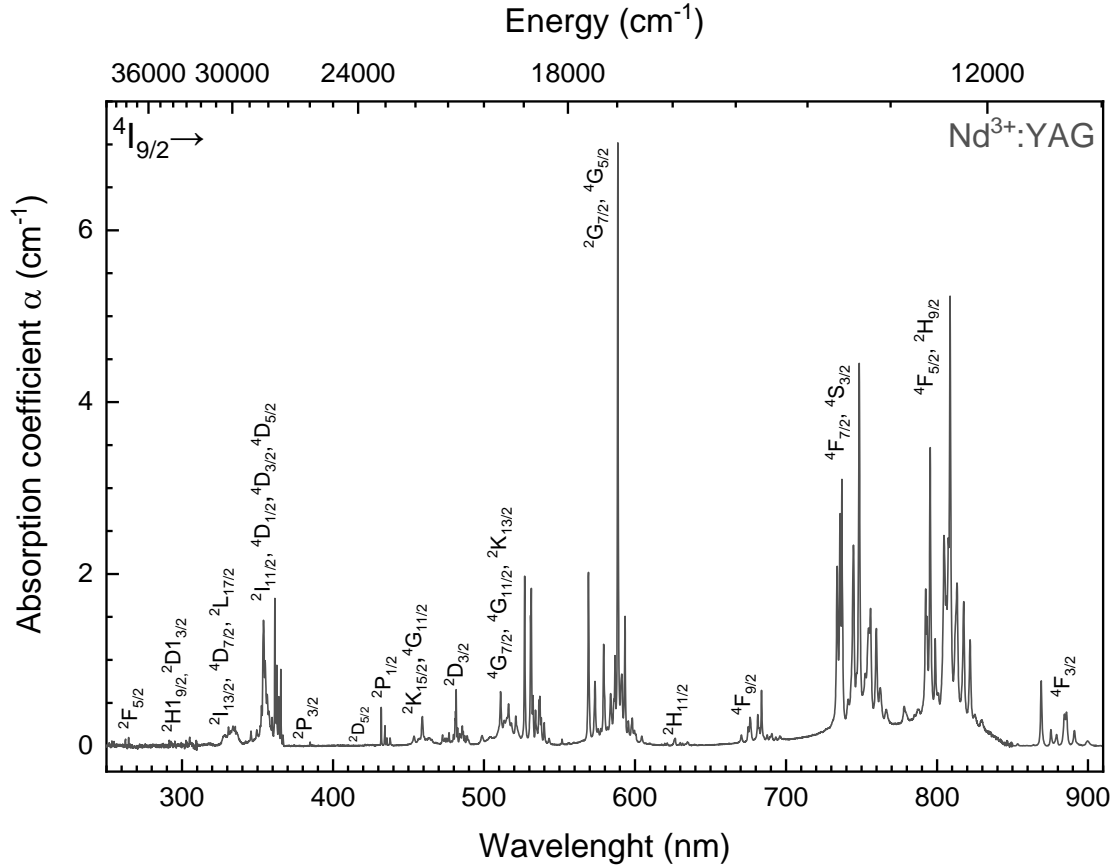
Figure 4. Absorption spectrum for Nd:YAG doped at 1% mol at ambient conditions.

In Table 3 are presented the line strengths according to Judd-Ofelt theory. As a group, the most perceptible are the transitions which have the largest areas, i.e., for Nd:YAG, the level $^4G_{5/2}$, $^2G_{7/2}$ at 586 nm has the highest α, but the highest line strength value corresponds to the band $^4F_{5/2}$, $^2H_{9/2}$, at 805 nm (taking the experimental line strength number), as well as with the other samples. The Nd:YAGG shows the highest ones, in the majority of transitions, where some of them are more than the double than the other samples. Comparing the root-mean square deviations, using the Carnall matrix elements [Carnall et al. 1968] gets a minor error for Nd:YAG and Nd:YAGG, whereas for Nd:YGG is the opposite of [Carnall 1978]. For Nd:YAGG, using the matrix elements of [Carnall 1978], is an order of magnitude larger than for the other calculations.

The calculated line strengths have strong differences using different Carnall matrix elements [Carnall 1978; Carnall et al. 1968], and those that coincide with the calculated line strengths are those that present larger matrix elements values, as the $^4G_{5/2}$, $^2G_{7/2}$, $^2K_{13/2}$ bands, at 526 nm, and the $^4G_{9/2}$, $^4G_{7/2}$, at 585 nm, because they play an important role in the fitting, Eq. (16), having in the contrary the worst fittings, i.e. for the level $^4F_{3/2}$, at 879 nm. Besides to this, for some transitions it is possible to separate them individually, not as a

combination of a few levels, having worse results, being a reason to use two different matrix elements. Another reason resides in that one of them, given in reference [Carnall 1978], do not include data for transitions above of $^2P_{3/2}$, and the difference of results obtained using different matrix elements for the same author can be interesting to be showed. For Nd:YGG and Nd:YAGG, it was not possible to analyze the UV transitions (from 250 nm to 300 nm), although it was for Nd:YAG. All transitions were not included in the fitting because some of them give rise to worse results.
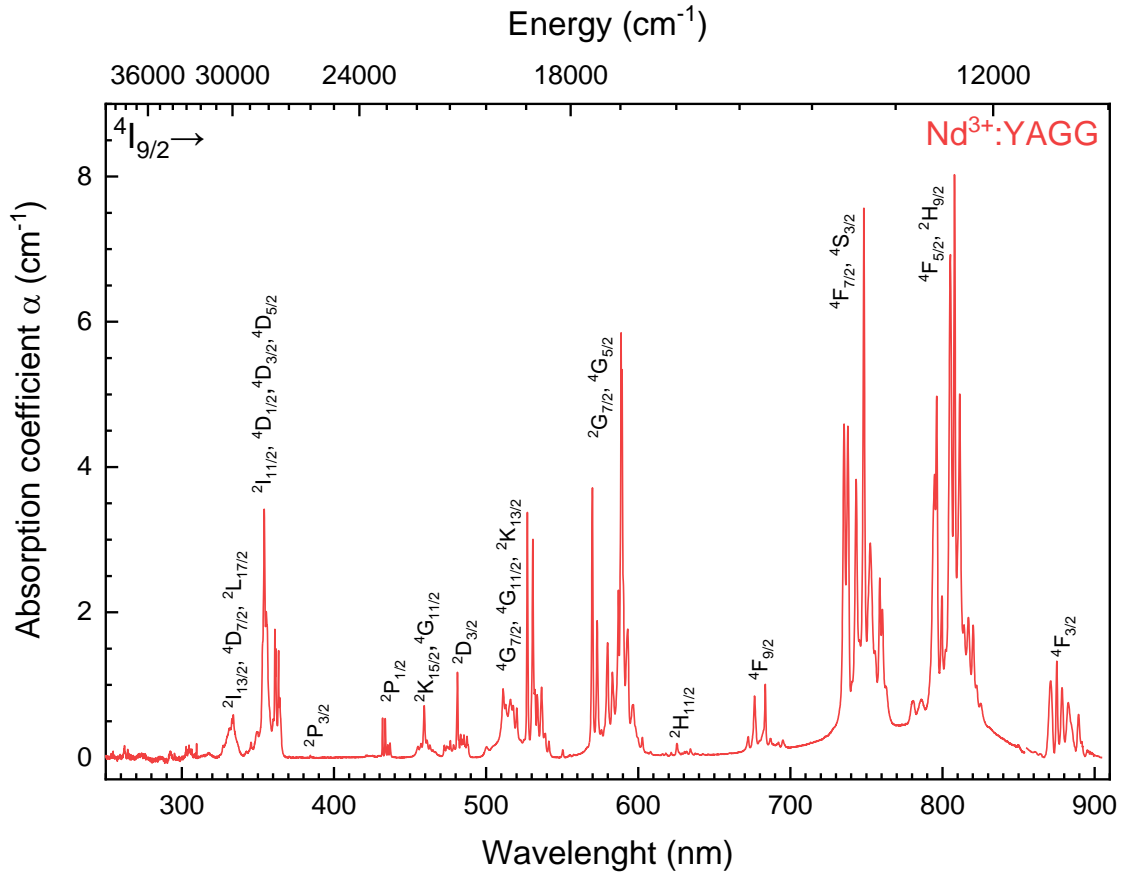

Figure 5. Absorption spectrum for Nd:YAGG doped at 1% mol at ambient conditions.

The program used to obtain the Judd-Ofelt parameters has been designed in Python programming language, resolving Eqs. (14) to (23), being checked successfully using different data [Walsh 2006; Krupke 1971], and obtaining similar values in both, where their intensity parameters Ω_t are shown in Table 4. The results presented by W. Krupke and J. Dong [Krupke 1971; Dong et al. 2005] (see in Table 4 the superscripts 3 and 4 for Nd:YAG) do not coincide with ours, especially for the Ω_2 parameter. Been said that negative Ω_2 values for Nd:YAGG and Nd:YGG are pointless, considering that the unique ion where it can be obtained is in *Pr*[3+] studies [Walsh 2006; Medeiros et al. 1995], they are low in magnitude enough to consider them closer to zero. This is another reason to use other matrix elements

such as those in reference [Carnall et al. 1968]. Since it was made an approximation in the refractive index in Nd:YAGG, the discrepancies in values can be understood considering that a slight change in constants as the refractive index, and in general, it can be produced by deviations in barycenters or areas, which they can utterly change all the results, giving different values, even for the intensity parameters. Another possibility to have got these values can be the device used to obtain the spectra, the integration wavelength ranges on the bands, the transitions identification, or even taken other bands beyond 900 nm.
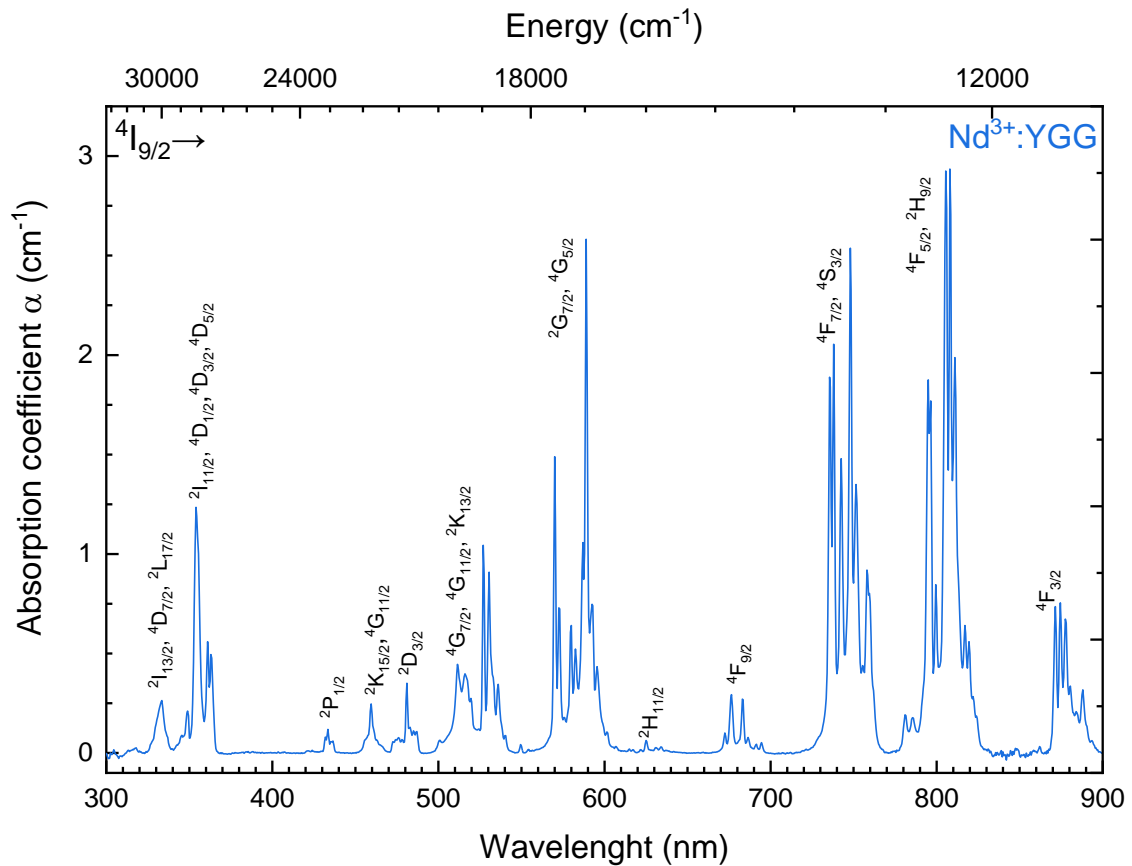

Figure 6. Absorption spectrum for Nd:YAG doped at 1% mol at ambient conditions.

Comparing the intensity parameters doing the arithmetical average of values which were obtained using the different matrix elements, and taking as reference Nd:YAG: for Nd:YGG Ω_4 and Ω_6 are the 50 % and 90 % respectively, and for Nd:YAGG Ω_4 and Ω_6 are the 30 % and 33 %. Not including the Ω_2 values on this discussion (considered null), it seems that Nd:YAGG differs much more than for the others, obtaining the highest values.

Table 3. Barycenter of the absorption bands, areas, experimental and calculated line strength values for Nd:YAG, Nd:YAGG and Nd:YGG. For the calculated line strengths, they were used different Carnall matrix element of references [1][Carnall 1978] and [2][Carnall et al. 1968].

Sample	Absorption $^4I_{9/2} \rightarrow$	$^2F_{5/2}$	$^2H_{9/2}$, $^2D1_{3/2}$	$^4I_{13/2}$, $^4D_{7/2}$, $^2L_{17/2}$	$^2I_{11/2}$, $^4D_{1/2}$, $^4D_{3/2}$, $^4D_{5/2}$	$^2P_{3/2}$	$^2D_{5/2}$	$^2P_{1/2}$	$^2K_{15/2}$, $^2G_{9/2}$	$^2D_{3/2}$	$^2K_{13/2}$, $^4G_{9/2}$, $^4G_{7/2}$	$^4G_{5/2}$, $^2G_{7/2}$	$^2H_{11/2}$	$^4F_{9/2}$	$^4F_{7/2}$, $^4S_{3/2}$	$^4F_{5/2}$, $^2H_{9/2}$	$^4F_{3/2}$
Nd:YAG	Baricenter $\bar{\lambda}$ (nm)	264	305	333	355	386	421	434	461	482	525	586	630	683	746	805	879
Nd:YAGG		-	-	333	354	385	-	433	461	482	527	585	630	682	747	807	879
Nd:YGG		-	-	334	357	-	-	434	459	482	525	583	627	681	746	805	878
Nd:YAG	$\int \alpha(\lambda)d\lambda$ (Å/cm)	0.3	0.8	18.4	75.9	0.2	0.8	4.4	15.6	20.8	112.8	178.9	3.4	42.1	400.6	487.1	31.4
Nd:YAGG		-	-	35.8	171.2	0.1	-	9.2	26.0	26.3	220.6	380.1	17.2	81.4	794.8	1011.0	112.1
Nd:YGG		-	-	16.8	80.1	-	-	5.2	11.6	16.4	109.0	186.1	4.7	21.1	282.7	350.7	230.3
Nd:YAG	S_{exp} ($\cdot 10^{-21}$ cm^2)	0	0	2	9	0	0	0	1	2	9	13	0	3	23	26	2
Nd:YAGG		-	-	7	30	0	-	1	4	5	27	42	2	8	70	83	8
Nd:YGG		-	-	3	14	-	-	1	2	2	14	21	0	2	25	29	18
Nd:YAG	$S_{calc}^{(1)}$ ($\cdot 10^{-21}$ cm^2)	-	-	-	-	0	0	0	1	0	8	13	0	1	20	20	1
Nd:YAGG		-	-	-	-	0	-	3	3	1	26	43	1	4	63	63	5
Nd:YGG		-	-	-	-	-	-	2	1	1	14	21	0	2	25	28	20
Nd:YAG	$S_{calc}^{(2)}$ ($\cdot 10^{-21}$ cm^2)	0	0	1	9	0	0	1	1	0	8	13	0	2	26	23	5
Nd:YAGG		-	-	2	31	0	-	2	3	1	26	43	1	5	79	71	17
Nd:YGG		-	-	0	18	-	-	1	1	1	12	21	0	2	27	27	9
Nd:YAG	Δrms							[1]$5 \cdot 10^{-21}$		[2]$3 \cdot 10^{-21}$							
Nd:YAGG								[1]$1 \cdot 10^{-20}$		[2]$6 \cdot 10^{-21}$							
Nd:YGG								[1]$1 \cdot 10^{-21}$		[2]$4 \cdot 10^{-21}$							

Table 4. Judd-Ofelt parameters. Matrix elements of references [1][Carnall 1978] and [2][Carnall et al. 1968] were used. For Nd:YAG, in italics, values correspond with references [3][Krupke 1971] and [4][Dong et al. 2005].

Judd-Ofelt intensity parameters	Nd:YAG				Nd:YAGG		Nd:YGG	
Ω_2 ($\cdot\,10^{-20}$cm^2)	0.01[1]	0.2[2]	*0.2[3]*	*0.6[4]*	-0.01[1]	0.6[2]	-0.3[1]	0.06[2]
Ω_4 ($\cdot\,10^{-20}$cm^2)	1.9[1]	1.4[2]	*2.7[3]*	*1.7[4]*	6.4[1]	5.0[2]	4.1[1]	3.0[2]
Ω_6 ($\cdot\,10^{-20}$cm^2)	3.0[1]	3.8[2]	*5.0[3]*	*5.8[4]*	9.1[1]	11.6[2]	3.5[1]	3.9[2]
Quality factor X (a.u.)	0.6[1]	0.4[2]	*0.5[3]*	*0.3[4]*	0.7[1]	0.4[2]	1.2[1]	0.8[2]

The X factor serves to study the spectroscopic quality for laser media [Kaminskii and Li 1974], using Eq. (18). According to the bibliography, for Nd:YAG we obtained similar values (see superscripts 1-4 in Table 4), although for Nd:YGG, X = 0.38 [Kaminskii and Li 1974], but in our case was obtained a value nearby to 1. In the case of Nd:YGG, the different values with the bibliography can be explained by the intensity parameters obtained, and on the contrary to reference, where they took only the $^2I_{15/2}$ and $^2P_{1/2}$ bands to do the calculations, in this case many other bands were taken into account in the fitting.

Luminescence measurements

For the luminescence study, $^4I_{9/2} \rightarrow {}^4F_{5/2}$, $^2H_{9/2}$ transitions at 805 nm were chosen to excite the samples, which corresponds with the largest line strength value. Emission spectra were measured in the range NIR, from 850 nm to 1460 nm, seeing three different de-excitation transitions from $^4F_{3/2}$, to the ground state, as $^4I_{9/2}$, and the excited states, $^4I_{11/2}$ and $^4I_{13/2}$ (see Fig. 7), being all of them corrected from the spectral response of both spectrophotometers.

As it can be seen in Fig. 7, it is beholden that all spectra present similar barycenter values, but seeing Table 5 they present slight shifts. For the $^4F_{3/2} \rightarrow {}^4I_{15/2}$ barycenter was taken from the arithmetic average of the values offered by references [Krupke 1971; Carnall 1978], because this emission range was not acquired. In the samples appear different number of peaks; i.e. for Nd:YAG, in the $^4F_{3/2} \rightarrow {}^4I_{9/2}$ transition, it can be counted ten peaks, but in Nd:YAGG can only been distinguished eight, and in Nd:YGG eleven peaks. Also it can be observed that emission spectrum for Nd:YAG, whose peaks are well distinguished, is different among Nd:YAGG and Nd:YGG, which they are pretty similar among them, and they present some overlapping phenomena in their peaks as opposed in Nd:YAG. It can be explained because there is a larger crystal-field interaction in Nd:YAG than in others [Lavín et al. 2015]. In Figs. 9 and 10 are presented, for Nd:YAG and Nd:YGG samples, the

experimental spectra and the values of the theoretical energy transitions given in reference [Morrison and Leavitt 1982] between the multiplets by Stark effect, being in red the ones which are not thermalized, while the others are.
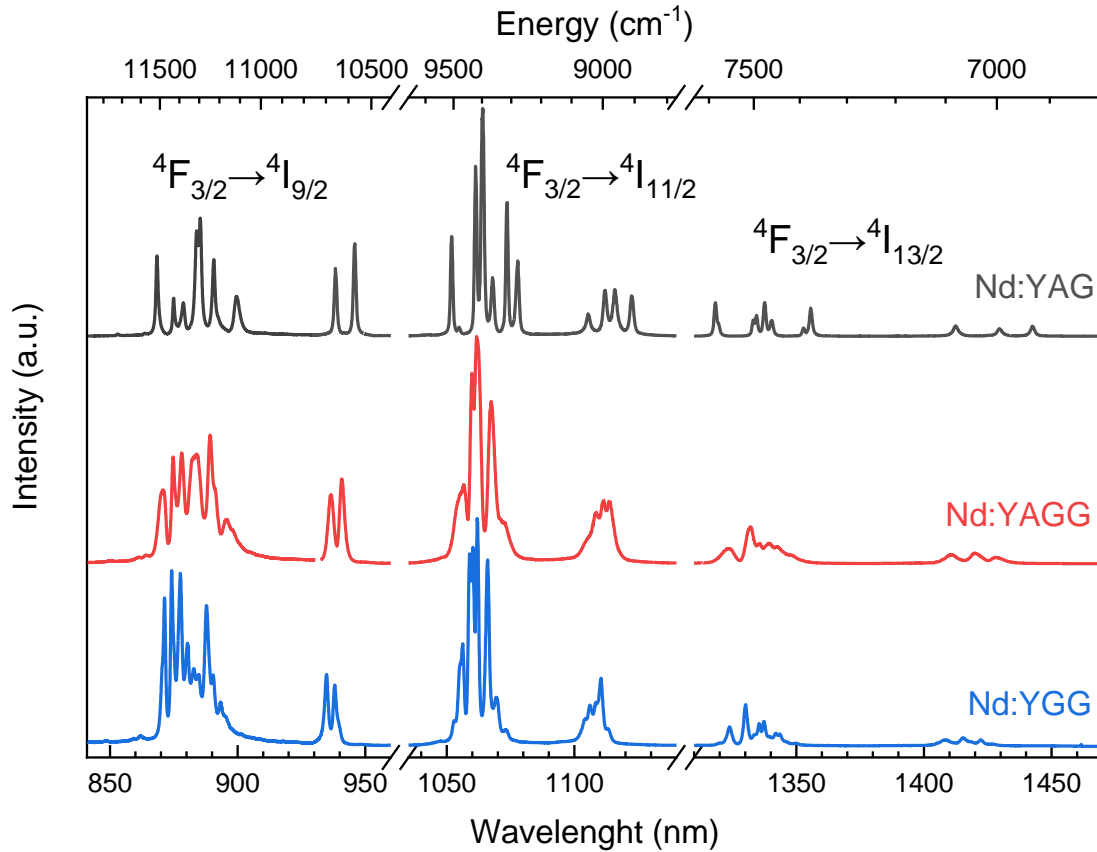

Figure 7. Normalized emission spectra for Nd:YAG, Nd:YAGG and Nd:YGG at ambient conditions, respectively. Transitions from $^4F_{3/2} \to {}^4I_{9/2}$, $^4F_{3/2} \to {}^4I_{11/2}$, $^4F_{3/2} \to {}^4I_{13/2}$, exciting the samples to the $^4F_{5/2}$, $^2H_{9/2}$ state with an 805 nm laser.

In Fig. 8 the energy level diagrams, as well as the radiative and non-radiative de-excitation processes are shown for Nd:YAG and Nd:YGG samples, taking their energies to build Figs. 9 and 10, whose spectral response are corrected in both cases. For Nd:YAG sample, in the $^4F_{3/2} \to {}^4I_{9/2}$ and $^4F_{3/2} \to {}^4I_{11/2}$ transitions were labelled according to the values from reference [Morrison and Leavitt 1982], calculating the differences among levels. However, in $^4F_{3/2} \to {}^4I_{13/2}$ transition, the furthest IR region they are only notorious three peaks well defined, identifying them correctly, but there are others values that could not be assigned, concretely for the $R_1 \to X_6$, $R_2 \to X_6$ and $R_2 \to X_7$ levels, because they could not be seen in the spectra, due to the overlapping peaks. In Fig. 9, all Stark peaks offered for the same bibliographic source are represented, but not for Nd:YGG sample (Fig. 10), having a larger overlapping phenomenon. For Nd:YAGG, there is not any bibliographic data of these Stark multiplets, for this reason there is not a peak identification.
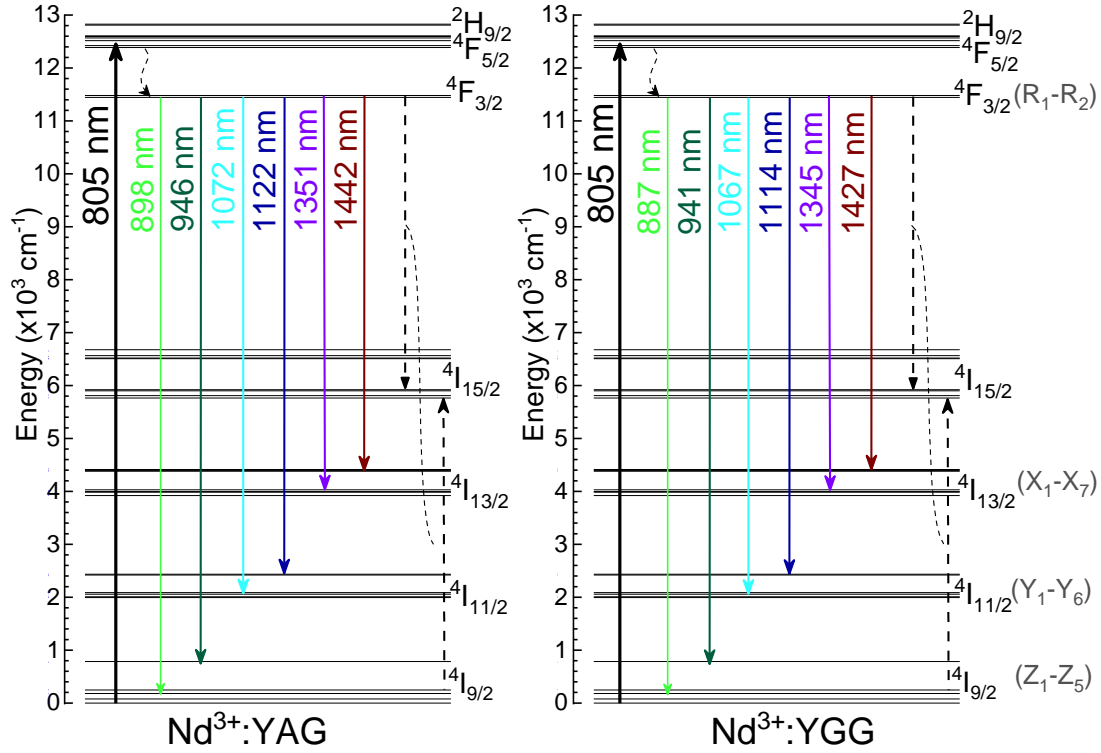
Figure 8. Partial energy level diagrams of the Nd³⁺ ion for radiative transitions, in red arrows, exciting it to the ²H₉/₂, ⁴F₅/₂ from the ground state ⁴I₉/₂, at 805 nm wavelegth. The non-radiative relaxation processes, as multiphonon and cross relaxation are shown in zig-zag and dashed arrows too. Left is for Nd:YAG. Right for Nd:YGG.

In Table 5 are presented the line strengths S_{ED}, spontaneous probabilities A_{ED}, branching ratios β, and the radiative lifetimes τ_{rad} which were calculated from the absorption data using Eqs. (20) to (23). It is necessary to consider that from the metastable $^4F_{3/2}$ level, the energy can be transferred to the lowest levels ^4I_J, $J=9/2$, …, 15/2, seen in the Dieke's diagram in reference [Carnall 1978]. They were obtained using the matrix elements given by references [Carnall 1978; Krupke 1971], having certain parameters which vary noticeably among different matrix elements employment, although the line strengths do not vary dramatically.

However, these little changes can produce big differences, i.e. in τ_{rad} of Nd:YGG, having a difference of 10 %; or in the spontaneous radiative transition rates, and branching ratios, where they even can change the most probable transition, like in the case of Nd:YGG, where $^4F_{3/2}{\rightarrow}^4I_{9/2}$ and $^4F_{3/2}{\rightarrow}^4I_{11/2}$ transitions are pretty similar among them, but they change in the way that considering the Carnall's matrix elements [Carnall 1978], the highest branching ratio is for $^4F_{3/2}{\rightarrow}^4I_{9/2}$, and considering the Krupke's ones [Krupke 1971], $^4F_{3/2}{\rightarrow}^4I_{11/2}$ transition presents the highest value. Studying Nd:YAG and Nd:YAGG branching ratios, $^4F_{3/2}{\rightarrow}^4I_{11/2}$ is the most probable transition in both of them, and taking a look to the

emission spectrum, it can be concluded that for Nd:YGG $^4F_{3/2}\rightarrow{}^4I_{11/2}$ is the most probable transition, and in consequence using the matrix elements from reference [Krupke 1971] offers a better fitting to the data. Perhaps this discrepancy in branching ratios for Nd:YGG can be explained because the difference among maximum intensities of $^4F_{3/2}\rightarrow{}^4I_{9/2}$ and $^4F_{3/2}\rightarrow{}^4I_{11/2}$ are minor than in other samples, whose intensities between these transitions are more separated.

Table 5. Barycenter values, line strengths, spontaneous radiative transition rates, branching ratios and radiative lifetimes of Nd:YAG, Nd:YAGG and Nd:YGG garnets. The *I* and *II* labels are given using the matrix elements of references [Carnall 1978; Krupke 1971], respectively; the $^4F_{3/2}\rightarrow{}^4I_{15/2}$ barycenter was taken using those references.

	Transition $^4F_{3/2}\rightarrow$	Barycenter (nm)	S_{ED} ($\cdot 10^{-21}\text{cm}^2$)		A_{ED} (s^{-1})		β		τ_{rad} (μs)	
			I	*II*	*I*	*II*	*I*	*II*	*I*	*II*
Nd:YAG	$^4I_{9/2}$	898	5	5	774	747	0.341	0.307		
	$^4I_{11/2}$	1072	15	16	1224	1312	0.538	0.538	440	411
	$^4I_{13/2}$	1351	6	9	262	367	0.115	0.151		
	$^4I_{15/2}$	1814	1	1	14	11	0.006	0.004		
Nd:YAGG	$^4I_{9/2}$	896	20	18	3094	2783	0.380	0.332		
	$^4I_{11/2}$	1077	46	49	4171	4379	0.511	0.523	123	119
	$^4I_{13/2}$	1365	19	27	840	1178	0.103	0.141		
	$^4I_{15/2}$	1814	3	9	48	35	0.006	0.004		
Nd:YGG	$^4I_{9/2}$	887	11	9	2017	1619	0.477	0.416		
	$^4I_{11/2}$	1067	18	18	1835	1854	0.434	0.476	237	257
	$^4I_{13/2}$	1345	8	9	362	409	0.086	0.105		
	$^4I_{15/2}$	1814	1	1	11	13	0.003	0.003		

Related to the difference of τ_{rad} between samples, the lowest value was calculated for Nd:YAGG and comparing among the other samples, for Nd:YGG is almost the double, and for Nd:YGG is the triple. This discrepancy can be related with the ion and the crystal-field interaction, and the intrinsic uncertainty in the estimation for the intensity parameters Ω_t. In regard to the line strengths, and their spontaneous probabilities for the $^4F_{3/2}\rightarrow{}^4I_{15/2}$ transition, low intensity bands are expected as can be seen for the energy diagrams (Fig. 8), showing the non-radiative de-excitation mechanisms for Nd:YAG and Nd:YGG. So, it can be concluded that the most probable transitions are $^4F_{3/2}\rightarrow{}^4I_{11/2}$ and $^4F_{3/2}\rightarrow{}^4I_{9/2}$, followed by $^4F_{3/2}\rightarrow{}^4I_{13/2}$. In addition, an upconversion study for the three samples was done, exciting them at 805 nm. In these hosts they were not found any evidence of this process in the visible range, because if it was produced, it should have seen an intense white light, denotating the photon emission at different energies, as it can be seen in Fig. 11.
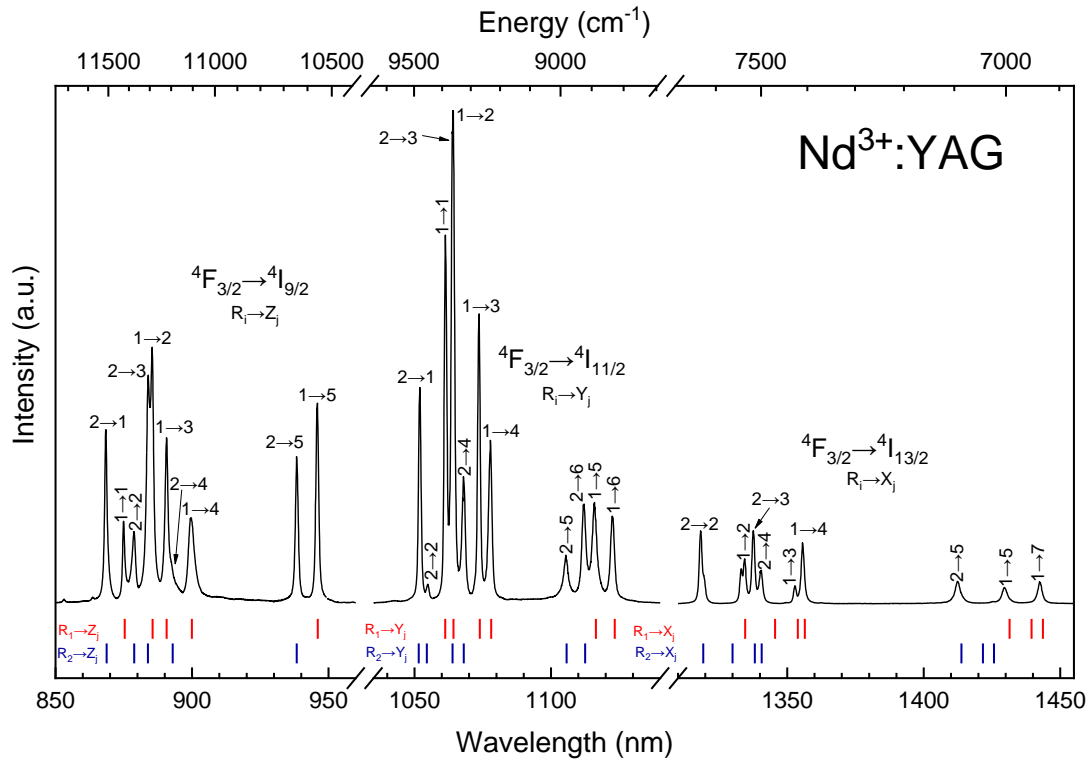
Figure 9. Emission spectrum at ambient conditions for Nd:YAG sample, exciting in 805 nm wavelength. In blue and red, theoretical transitions for each peak obtained from Stark effect.
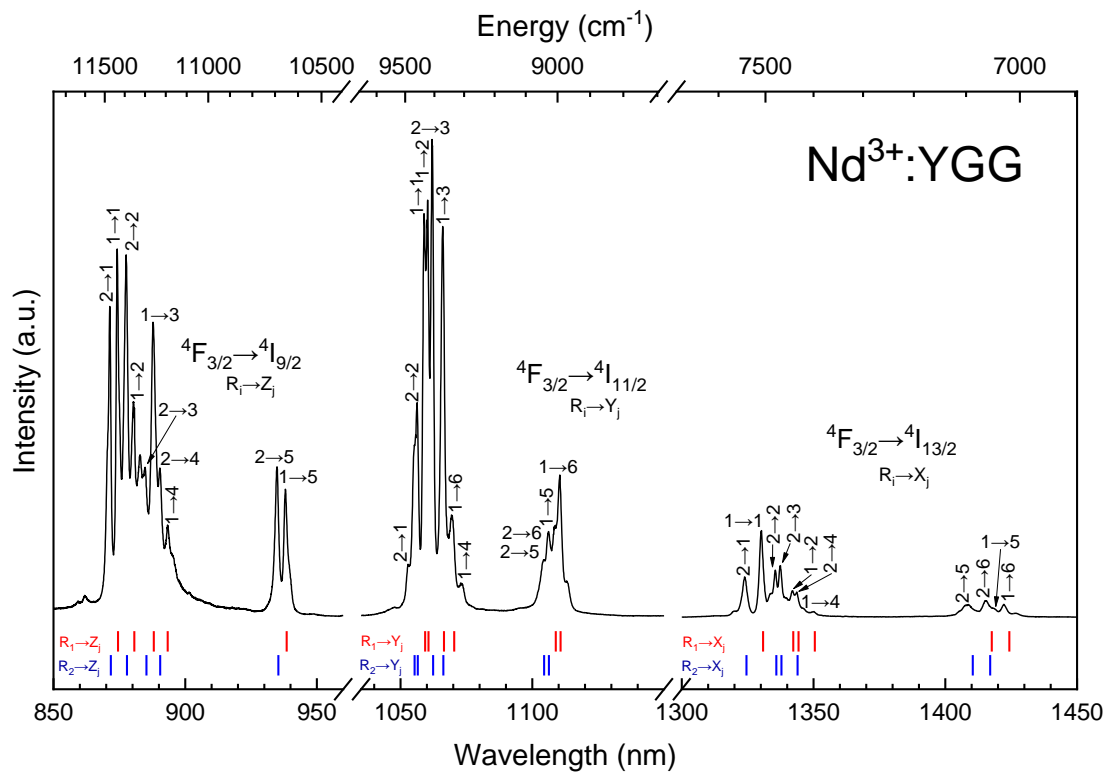

Figure 10. Emission spectrum at ambient conditions for Nd:YGG, exciting in 805 nm wavelength. In blue and red, theoretical transitions for each peak obtained from Stark effect.
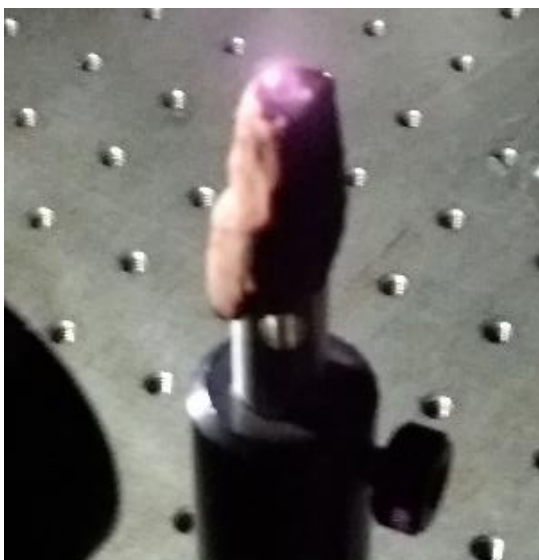
Figure 11. Nd:YAGG being excited at 805 nm to study the upconversion process in the visible range.

Lifetime measurements

Lifetime is the constant related with the emission probability seen in Eq. (24), having that the lattices where the ions are embedded, or the doping ion concentration will modify this constant, as well as external factors as the temperature or pressure. The lifetime constants were analyzed from the de-excitation curves obtained (see Fig. 12), exciting with the OPO to the $^4I_{9/2} \rightarrow ^4F_{5/2}$, $^2H_{9/2}$ band to then decay to $^4F_{3/2}$ level, and from there to the ground state. The time necessary for the intensity reaches e^{-5} units is almost the same for the three samples, around 1250 µs, and they seem to be almost exponential behaving, not being strictly that, especially at short times after a laser pulse, indicating the presence of energy transfer processes in the de-excitation. So, the data were fitted to the Inokuti-Hirayama model, given by Eq. (29), letting as free parameters the lifetime τ_0 and the Q factor, while S factor was fixed considering the electric-dipole mechanisms are the most likely ($S = 6$), because it was studied other multipolar contributions ($S = 8, 10$), but the fittings did not change noticeable among them. Usually τ_0 is fixed in the Inokuti-Hirayama expression, although in this case was preferred to let it vary freely.
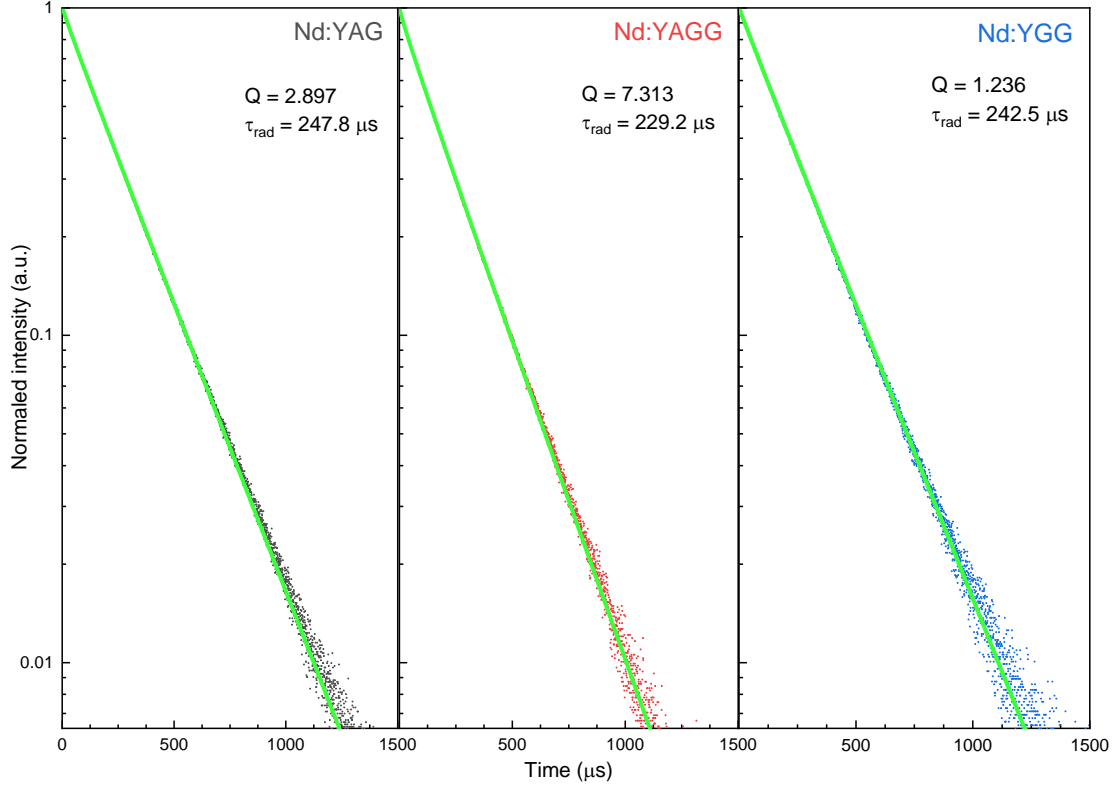
Figure 12. Decay curves at ambient conditions for $^4F_{3/2} \rightarrow {}^4I_{9/2}$ for Nd:YAG, Nd:YAGG and Nd:YGG garnets. In green, fitted curves to the Inokuti-Hirayama model with *S*=6.

In addition to this, the experimental times τ_{exp} were obtained using Eq. (25), where the results are depicted in Table 6. All of them show different time constants, being the lowest for Nd:YAGG with 215 μs, and the highest for Nd:YGG, with 241 μs, indicating that the lattice plays an important role in the de-excitation process. It seems like garnets which have a combination of aluminum atoms tend to reduce their lifetimes, meanwhile gallium atoms permit increase it, but if there is a combination of gallium and aluminum, the lifetime reduces even more, seen in Nd:YAGG. Observing the Inokuti-Hirayama lifetimes τ_0, the values are approaching with the experimental ones, being the closest value for Nd:YGG. For Nd:YAG, the average lifetime τ_{rad} given by the results by using the different matrix elements on the Judd-Ofelt calculations is 426 μs, almost twice than the Inokuti-Hirayama τ_0, having for the other samples an important difference among these values. Observing a datasheet of Advatech, τ_{rad} is around 550 μs, differing our value at 23 % [Advatech Web]. For Nd:YAGG, τ_{rad} is almost the half, being unclear this result, because it is usual that this lifetime was larger or equal than τ_{exp}, likely correlated by the big uncertainty in the Judd-Ofelt parameters. For Nd:YGG is the only sample where all lifetimes are approximately the same, being τ_{rad} larger than the experimental.

Comparing τ_{rad} with τ_{exp} to the quantum efficiency η_q, Eq. (26), observing that for Nd:YAGG presents the largest value at 178 %, being physically impossible because for τ_{exp} are included all de-excitation mechanisms, radiative and non-radiative ones, so it should be expected a shortening in this lifetime. For Nd:YGG is 98 %, while for Nd:YAG is 56 %.

Table 6. Lifetimes of garnets studied for transition $^4F_{3/2} \rightarrow {}^4I_{9/2}$. The τ_{exp} are the experimental lifetimes, meanwhile the I-H: τ_{rad} is given by the Inokuti-Hirayama fitting and J-O: τ_{rad} are the values obtained by Judd-Ofelt theory, taking the arithmetic average to results using the different matrix elements of Carnall [Carnall 1978; Carnall et al. 1968].

	Nd:YAG	Nd:YAGG	Nd:YGG
τ_{exp} (µs)	238 ± 1	215 ± 4	241 ± 1
$I - H: \tau_0$ (µs)	248	229	243
$J - O: \tau_{rad}$ (µs)	426	121	247

About the Q factor given in the fittings, is presented in Table 7. From Eq. (30), the critical transfer distance R_0 can be evaluated, and the donor-acceptor transfer parameter by Eq. (31). The most difference is observed for Nd:YAGG sample, with 1.6 times larger than other samples. Seeing the results obtained in the reference [Lavín et al. 2015], the result of R_0 in Nd:YGG nano-garnet is 3.8 Å, while the result of Nd:YGG garnet is 12.6 Å. For Nd:YAG and Nd:YGG are pretty similar among them, possibly if an error analysis was done, both values would go into each other error.

Table 7. Q factor, donor-acceptor transfer parameter and critical transfer distance for the samples.

	Nd:YAG	Nd:YAGG	Nd:YGG
Q factor	2.99	7.31	1.24
C_{DA} ($\cdot 10^{-40}$ cm^6/s)	0.08	1.26	0.04
R_0 (Å)	14.3	22.4	12.6

Extreme conditions

Low temperature measurements

This section is restricted to study Nd:YAG emission with temperature, in order to stablish this material as a temperature sensor. The sample was pumped with at 532 nm (18797 cm^{-1}) to the combination of states $^2K_{13/2}$, $^4G_{7/2}$, $^4G_{9/2}$, decaying by multiphonon de-excitation to the metastable $^4F_{3/2}$ level, and from this state to the ground state $^4I_{9/2}$. The

emission spectra as a function of temperature from 12 K to 250 K, has been presented in Fig. 13.

When the sample is cooling down, it can be observed an important decrease of the intensity of the $R_2 \rightarrow Z_i$ peaks, i=1-5, being not perceptible at the lowest temperature (it is seen that in the 50 - 12 K range they vanish gradually). As the $R_{1,2}$ levels are in thermal equilibrium following the Boltzmann's Law, at low temperatures the populations are mainly in the R_1 level, because the electrons cannot be promoted from R_1 to R_2, as occurs at higher temperatures, and in consequence emission from R_2 level become negligible. This is a good method to confirm peaks identified in the luminescence discussion. Another interesting point is the peaks centered at 893.5 nm and 905.5 nm respectively, being more intense at lower temperatures, that have not been identified yet.
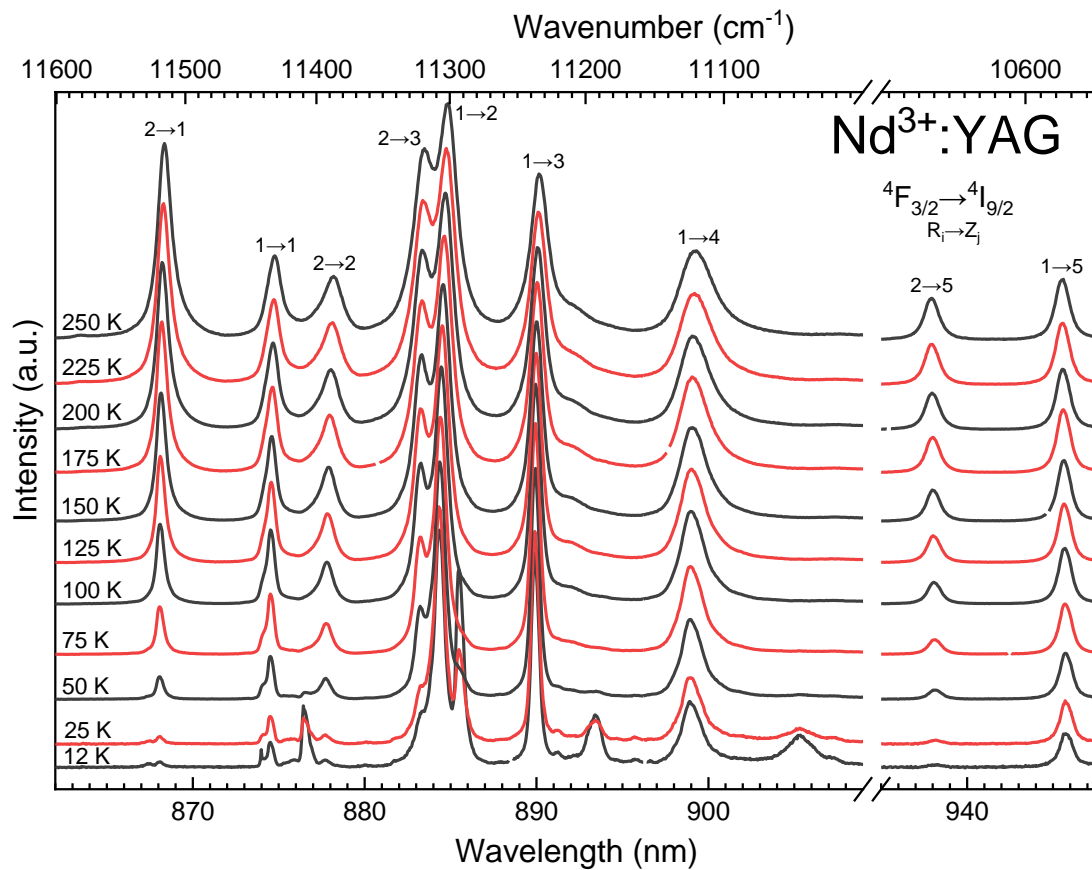

Figure 13. Normalized emission spectra series varying the temperature in Nd:YAG garnet, exciting in 532 nm, to the $^2K_{13/2}$, $^4G_{7/2}$, $^4G_{9/2}$ band.

As it said earlier, some temperature induced changes in the spectra in this sample can be used as a temperature scale, applying the LIR technique. In this case, it is focused on the peaks $R_2 \rightarrow Z_5$ (E_{31}) and $R_1 \rightarrow Z_5$ (E_{21}) transitions. The energy gap ΔE ($E_{31} - E_{21}$) between these peaks has been experimentally calculated using the spectra in Fig. 13,

$\Delta E = E_{31} - E_{21} = 86 \text{ cm}^{-1}$ remaining constant, as well as the integrated relative intensities of these bands denoted as I_{31} and I_{21} in Eq. (32). The results were treated according to:

$$\ln R = \ln C - AT^{-1} \tag{38}$$

being R the ratio peaks; $A = \text{d} \ln R/\text{d}T$ the slope, corresponding with $A = \Delta E/k_B$; C is the pre-exponential factor in Eq. (33); and the variable T^{-1} is the temperature inverse.
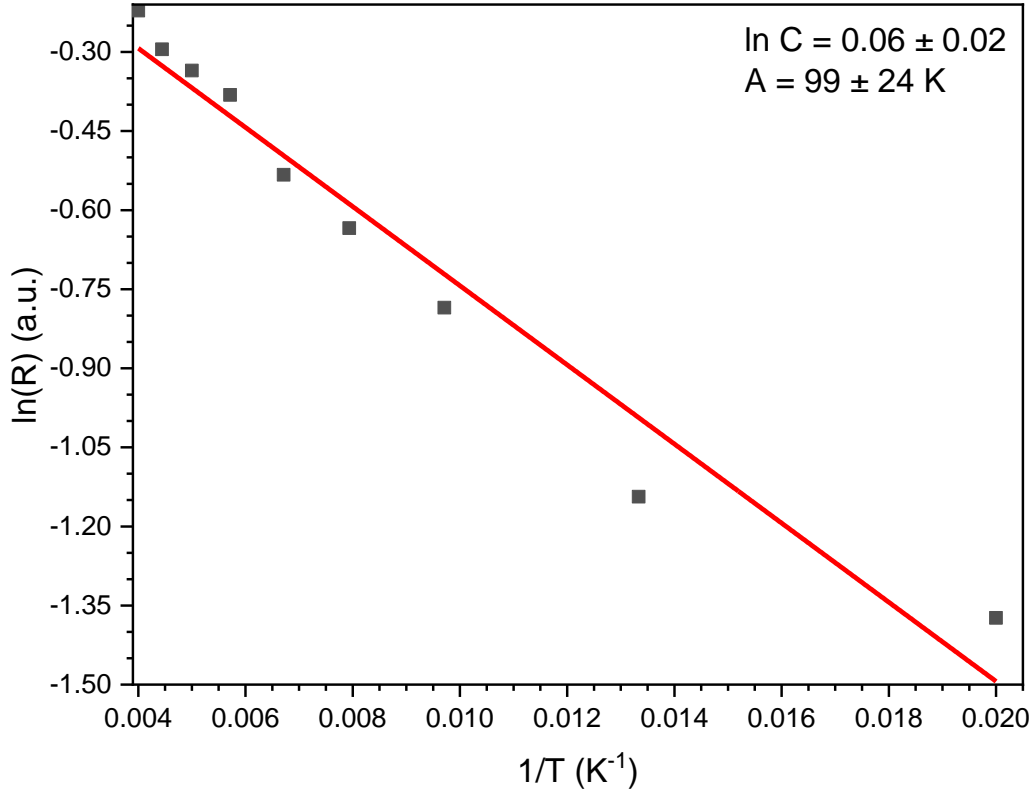

Figure 14. Experimental data and fitting curve (in red) to the Boltzmann distribution for Nd:YAG for LIR study.

According to the fitting, see Fig. 14, the energy gap is $71 \pm 17 \text{ cm}^{-1}$, and comparing the energy gap calculated experimentally in the spectra ($\Delta E = 86 \text{ cm}^{-1}$), they deviate by around 17 %, presenting a little difference among them, although both are in the error range. It is necessary to explain that the lowest temperature data were not taken into account for the fitting procedure because they give rise to a larger errors, because when the sample is warming up, the temperature could not be accurate controlled, increasing quickly in the 12-50 K range meanwhile the spectra were acquiring. A calculation was done to obtain the absolute and relative sensitivities (Fig. 15) using Eqs. (34) and (35), with the parameters obtained in the previous fitting. Observing the right plot, the sensitivity is not too high (0.0058 K⁻¹ at maximum), having the highest sensitivity at 49.5 K, and for the relative sensitivity in the left plot, this value decreases while temperature is increasing.
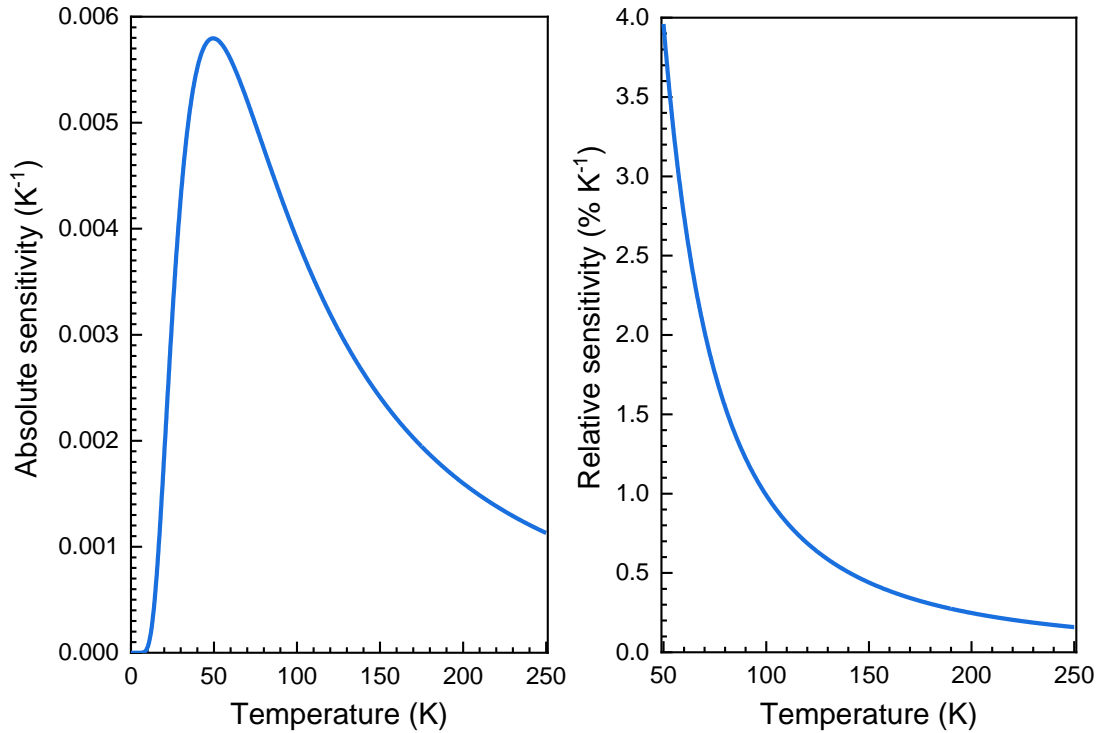
31

Figure 15. Left: absolute sensitivity, right: relative sensitivity, for the same temperature range taken in the LIR analysis, whose parameters of the fitting were used to obtain these curves.

High pressure measurements

In this section the emission as a function of pressure for Nd:YAG and Nd:YAGG samples will be presented, exciting the ruby chips at 532 nm laser (18800 cm^{-1}) while the samples were excited at 785 nm (12740 cm^{-1}) to the transitions $^4F_{5/2}$, $^2H_{9/2}$, decaying to the $^4F_{3/2}{\rightarrow}^4I_{9/2}$, $^4I_{11/2}$ levels.

As a general behavior, when pressure increases, the redshifts of the multiplets are observed, as well as a decrease of the emission intensity. In Figs. 16 and 17 are shown the spectra collection for Nd:YAG and Nd:YAGG, being labelled at ambient conditions the peaks of the first, according to the same notation used in the luminescence subsection. In all spectra the values were normalized by their maximum intensity in each transition, for this reason the maximums of $R_i{\rightarrow}Z_j$ and $R_i{\rightarrow}Y_j$ seem to be equally intense.

In both samples, (see Figs. 16 and 17) it is observed a losing in the profile of the peaks while pressure is increasing, i.e. for Nd:YAG they are well separated, but at higher pressures they are much wider, overlapping among them, being the identification much more difficult than at ambient conditions.
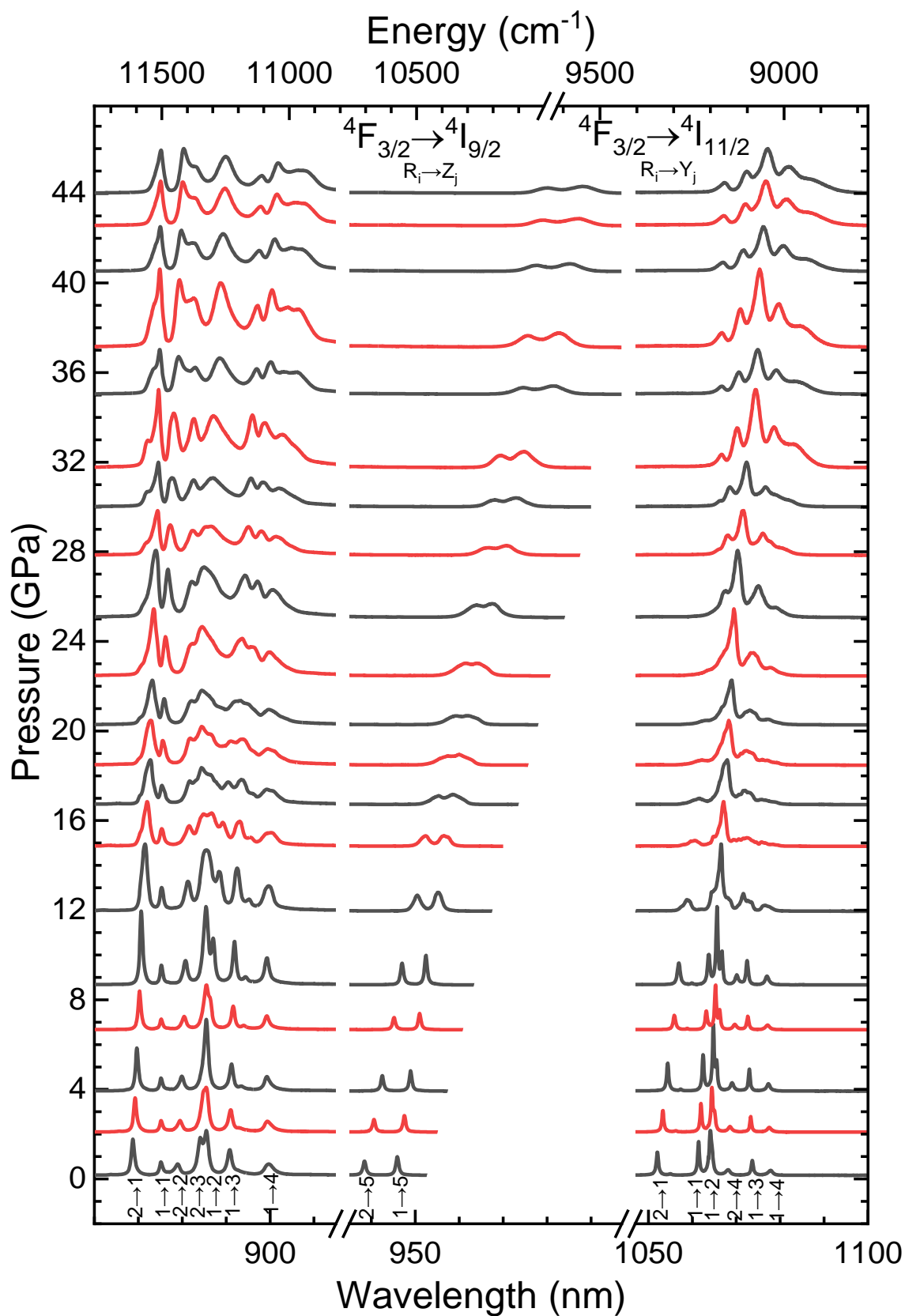
Figure 16. Normalized Nd:YAG spectra varying the pressure from 0.16 GPa to 44 GPa, exciting with a 785 nm laser for the transitions $^4F_{3/2} \rightarrow {}^4I_{9/2}$, from 850 nm to 1000 nm and for $^4F_{3/2} \rightarrow {}^4I_{11/2}$ from 1040 nm to 1150 nm.
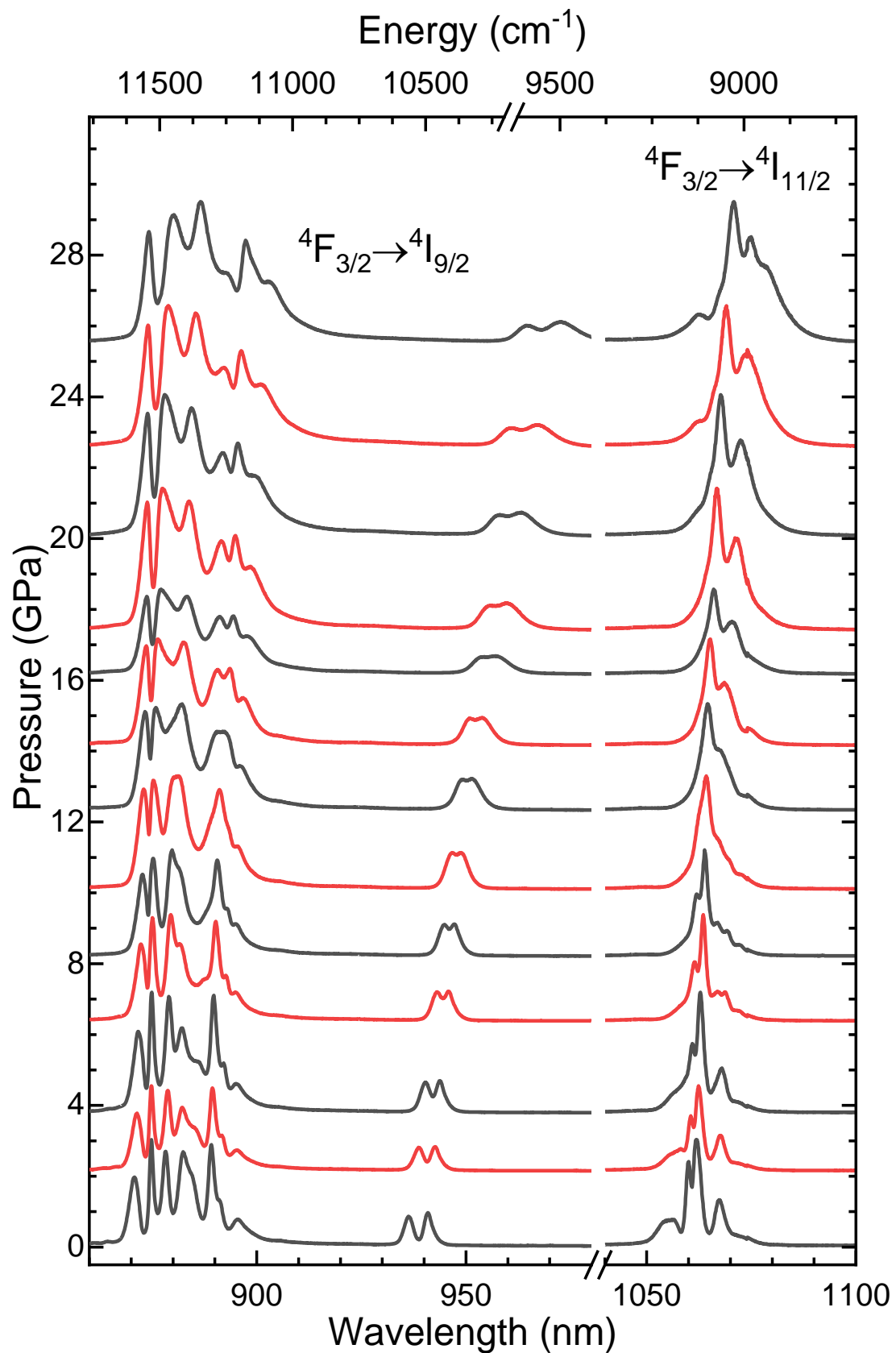
Figure 17. Nd:YAGG emission spectra obtained varying pressure from 0.03 GPa to 25.5 GPa, exciting with a 785 nm laser for the transitions $^4F_{3/2} \rightarrow {}^4I_{9/2}$, from 850 nm to 1000 nm and for $^4F_{3/2} \rightarrow {}^4I_{11/2}$ from 1040 nm to 1150 nm.

In particular, the focus will be on the $R_{1,2} \rightarrow Z_5$ transitions for both hosts, considered the best candidates for pressure sensing applications, because they are less affected by overlapping phenomena from other peaks and they have enough emission intensity at high pressure. As it was said in the luminescence subsection, the Nd:YAGG transitions could not be identified. However, $R_{1,2} \rightarrow Z_5$ transitions can be clearly distinguished, as it can be observed, so they will be used for sensor purposes. The peak positions were fitted to Lorentzian, whose results are depicted in Figs. 18 and 19. At first glance, the behavior of the energy peaks with pressure does not follow a linear tendency (see right plots), beholding that there is a pressure for which the peaks have the closest approach, at 20 GPa for Nd:YAG and at 12 GPa for Nd:YAGG, approximately, becoming to separate again. In the case of $R_1 \rightarrow Z_5$ it is more noticeable this lack of linearity. In the left plots of the same figures, it can be observed that when they are separating again are affected with overlapping phenomena, as said. In Table 8, linear fittings for the samples are presented, corresponding $d\lambda(R_i \rightarrow Z_5), i = 1,2$ with the wavelength infinitesimal increment for each multiplet labelled earlier, and dP the infinitesimal increment of pressure.
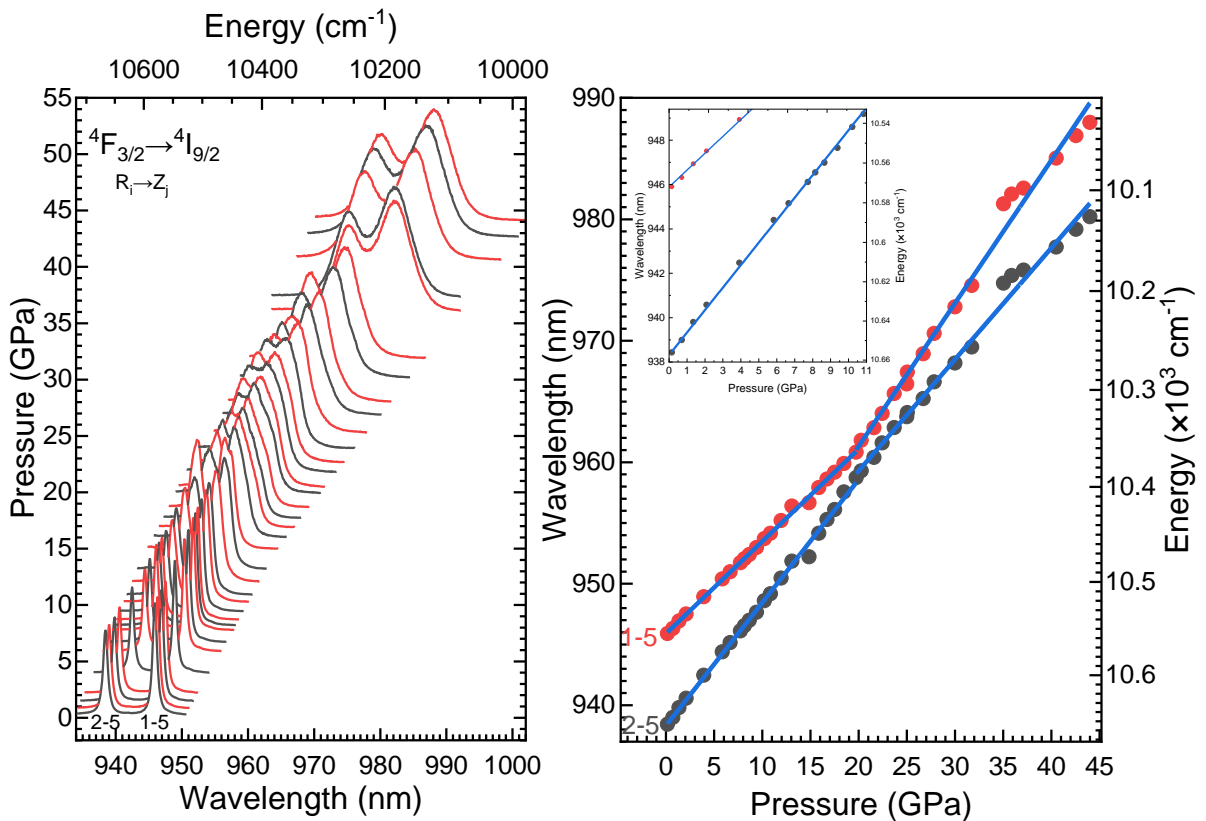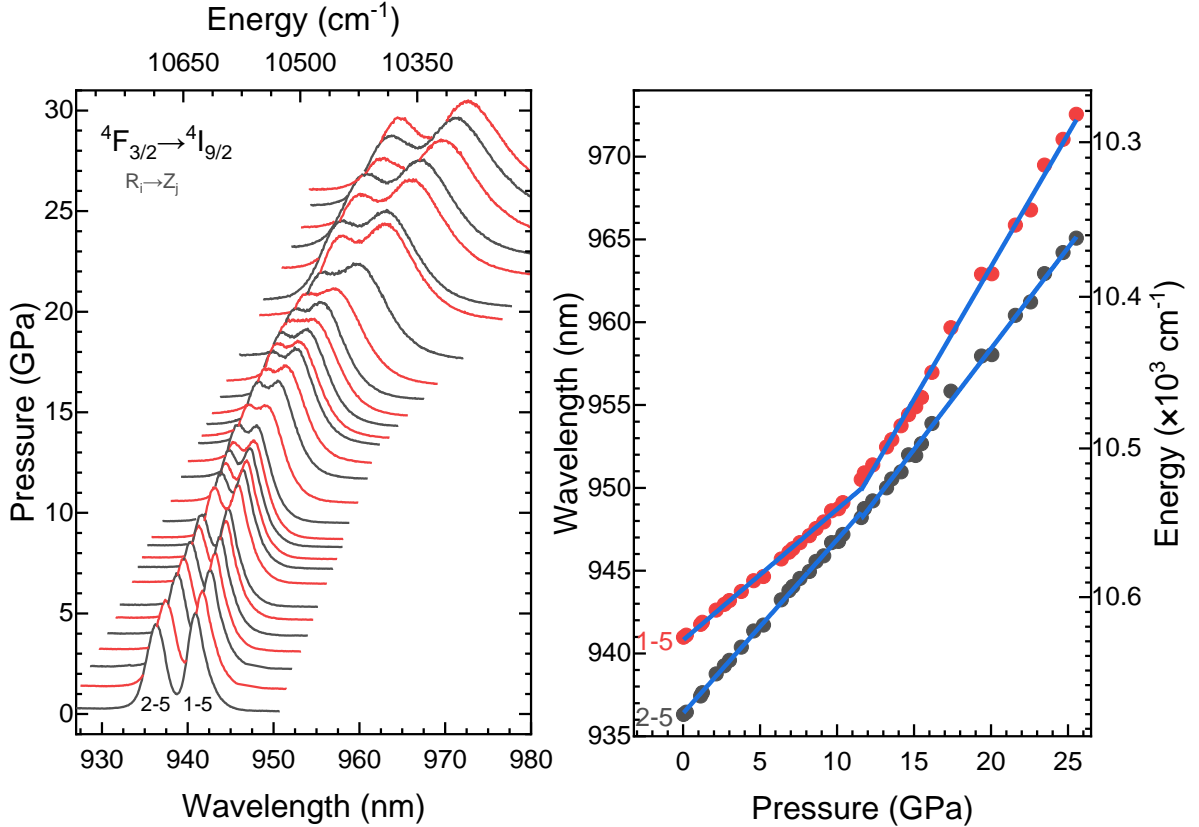

Figure 18. Nd:YAG $R_{1,2} \rightarrow Z_5$ intensity peaks for the $^4F_{3/2} \rightarrow ^4I_{9/2}$. Left: spectra of the peaks from ambient conditions to 44 GPa. Right, wavelength versus pressure plot at room temperature, with linear fittings in blue at different pressure ranges. Inset plot is the zoomed fitting of $R_1 \rightarrow Z_5$ from 0-11 GPa.

Table 8. Nd:YAG and Nd:YAGG slopes for the peaks R$_{1,2}$→Z$_5$ at different ranges varying the pressure at room temperature.

Sample	Pressure range (GPa)	d$\lambda(R_1 \rightarrow Z_5)$/dP (nm/GPa)	d$\lambda(R_2 \rightarrow Z_5)$/dP (nm/GPa)
Nd:YAG	$0-20$	0.760 ± 0.007	1.01 ± 0.01
	$20-44$	1.18 ± 0.03	0.92 ± 0.02
Nd:YGG	$0-11.6$	0.79 ± 0.01	1.05 ± 0.01
	$11.6-25.5$	1.60 ± 0.03	1.22 ± 0.02

Figure 19. Nd:YAGG R$_{1,2}$→Z$_5$ intensity peaks for the ^{4}F$_{3/2}$→^{4}I$_{9/2}$. Left: spectra of the peaks from ambient conditions to 44 GPa. Right, wavelength versus pressure plot at room temperature, with linear fittings in blue at different pressure ranges.

The results of Table 8 bear out that the R$_2$→Z$_5$ slopes vary faster than R$_1$→Z$_5$ before the closing, the opposite occurring after it. For Nd:YAGG were obtained more pronounced slopes than for Nd:YAG, meaning that the levels shift to lower energies faster, having the maximum approaching earlier for Nd:YAGG, at 11.6 GPa than for Nd:YAG, at 20 GPa. Also, for Nd:YAG there is a value for the R$_1$→Z$_5$ slope where it can be found in the reference [Recio et al. 2016], showing 0.87 nm/GPa, and in this case the measured pressure range is until 11 GPa, although the value obtained in this work differs by 14 % (1.00 $\pm$ 0.01 nm/GPa if it is only taken data until 11 GPa), not being within the statistical uncertainty, and not knowing

the reason of this discrepancy. Besides to this, there is another study for Nd:YAG [Rodríguez-Mendoza et al. 2013] where it shows that the slope for the peak $R_1 \rightarrow Z_5$ is -8.6 cm^{-1}/GPa and for $R_2 \rightarrow Z_5$ is -9.9 cm^{-1}/GPa. Treating conveniently the data, in this work the values obtained are -8.6 cm^{-1}/GPa and -11.27 cm^{-1}/GPa, respectively, at pressures below 20 GPa.

To conclude, it is obvious that there are a lot of possible peaks to be taken as a pressure sensor, but it is necessary to choose the best ones which could be easily identified according increases pressure. To illustrate this problem, it was done an analysis to the most intense peak for the $^4F_{3/2} \rightarrow ^4I_{11/2}$ transition, realizing that its profile changes more noticeably at different pressures, having in Fig. 20 the plot of the peak energy versus pressure for Nd:YAG and Nd:YAGG. The behavior of these peaks does not seem to follow a linearity, probably caused because other peaks overlap with it, changing the barycenter, not being recommendable for sensing applications.
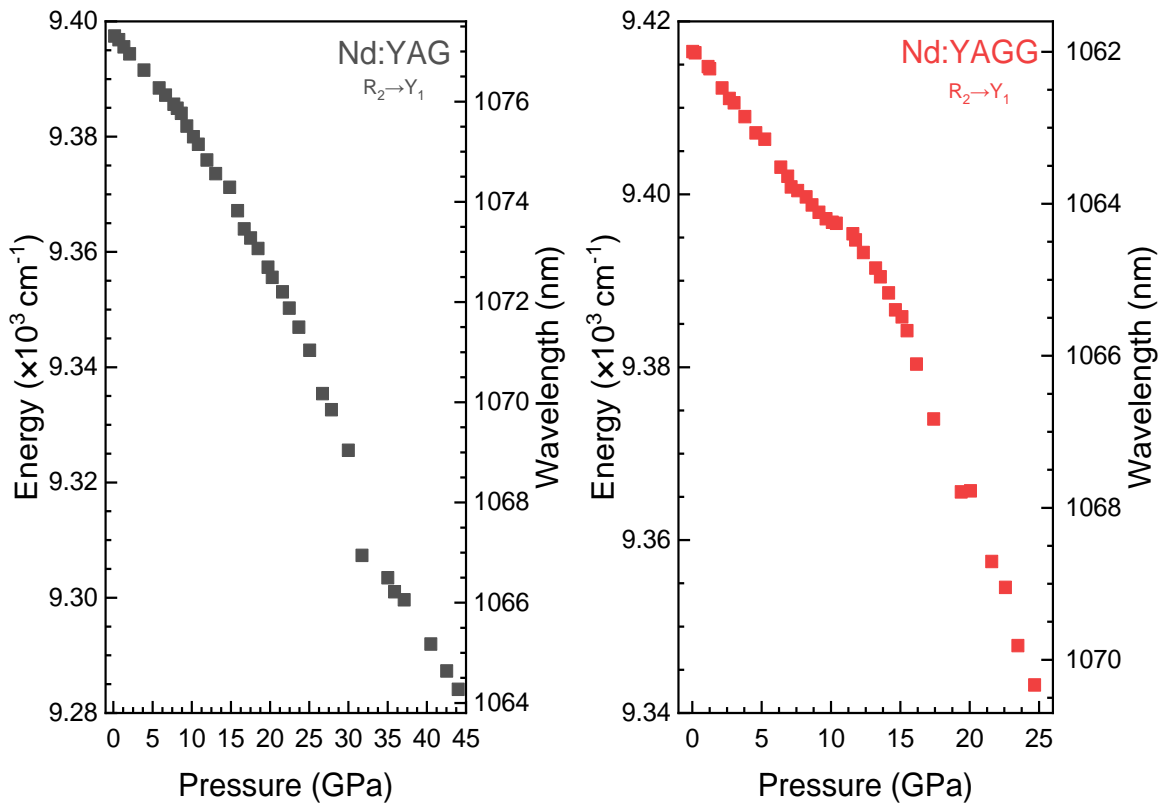

Figure 20. Left, Nd:YAG maximum peaks for $^4F_{3/2} \rightarrow ^4I_{11/2}$ transition. Right, maximum peaks for the most intense multiplet, for Nd:YAGG.

4. Conclusions

At ambient conditions, an optical study for Nd:YAG, Nd:YAGG, and Nd:YGG was presented, including the Judd-Ofelt theory. A novel computer program written in Python programming language was elaborated, tested with the results found in the literature [Krupke 1971; Walsh 2006], showing slight discrepancies. The line strength values are different for all samples, having the largest ones for Nd:YAGG. The Judd-Ofelt intensity parameters and quality factors are different too, comparing the results of Nd:YAG for with the references [Krupke 1971; Dong et al. 2005], presenting slight differences among them. This study was made using two different matrix elements from the same author [Carnall et al. 1968; Carnall 1978].

For the luminescence spectra, it has been presented that the transitions are produced from $^4F_{3/2}$ to lower levels as $^4I_{9/2}$, $^4I_{11/2}$ and $^4I_{13/2}$, not being observed photon emission at levels upper $^4F_{3/2}$. The profiles change regarding to the samples, having a bigger overlapping in Nd:YAGG and Nd:YGG, while in Nd:YAG are more separated. For the peaks that make up the multiplet transitions, almost all of them could be identified in Nd:YAG and Nd:YGG emission spectra. About the branching ratios, obtained using the Judd-Ofelt theory, agree among the intensities observed in the experimental spectra. There was not any evidence in the hosts for upconversion processes. For the lifetime results, experimental and radiative lifetimes were compared among them, finding some deviations in the radiative lifetimes, and the quantum luminescence efficiency, attributed to the uncertainties of the Judd-Ofelt parameters, and presenting that the radiative lifetime for Nd:YAG presented in this work is closer to the reference [Advantech Web].

Regarding to temperature study, thermalized peaks were identified in Nd:YAG due to its behavior. The LIR technique used and the absolute as well as the relative temperature sensibilities were calculated, and they could be employed as T-sensor luminescent in the infrared range. For extreme pressure study, the luminescence spectra were achieved at 44 GPa for Nd:YAG 25.5 GPa Nd:YAGG, following a similar behavior for the peaks, finding that they present an energy closing in $R_{1,2} \rightarrow Z_5$ multiplets, which were done a few linear fittings, giving the shifting rates for these peaks with pressure at different ranges. The good signal and the easy way to obtain information needed of these peaks permits to use them as a P-sensor luminescent in the infrared range.

5. Future projects

One of the most necessary item on the agenda is a deeper analysis for the Judd-Ofelt results, like the line strengths and the crystal intensity parameters, presented in the absorption subsection, taking other programs made for this proposal, or revising the parameters introduced in the programs, i.e. the areas, or the generation of new matrix elements. In relation with the Judd-Ofelt results, joined with the absorption and emission spectra, they can be used to obtain more useful parameters as the integrated absorption cross-section of the acceptor Q_A, the emission cross-section $\sigma_e(\lambda)$ or the optical gain cross-section $G(\lambda)$, among other parameters, as it presents in the reference [Rodríguez-Mendoza et al. 2011]. For lifetime discussion, it would interesting to do a deeper analysis about the decay processes which are involved between the samples, and this optical comparison could be extended introducer other garnets as Nd:LuGG or Nd:GGG, whose chemical formulas are $Lu_3a_5O_{12}$ and $Gd_3Ga_5O_{12}$ respectively, among others.
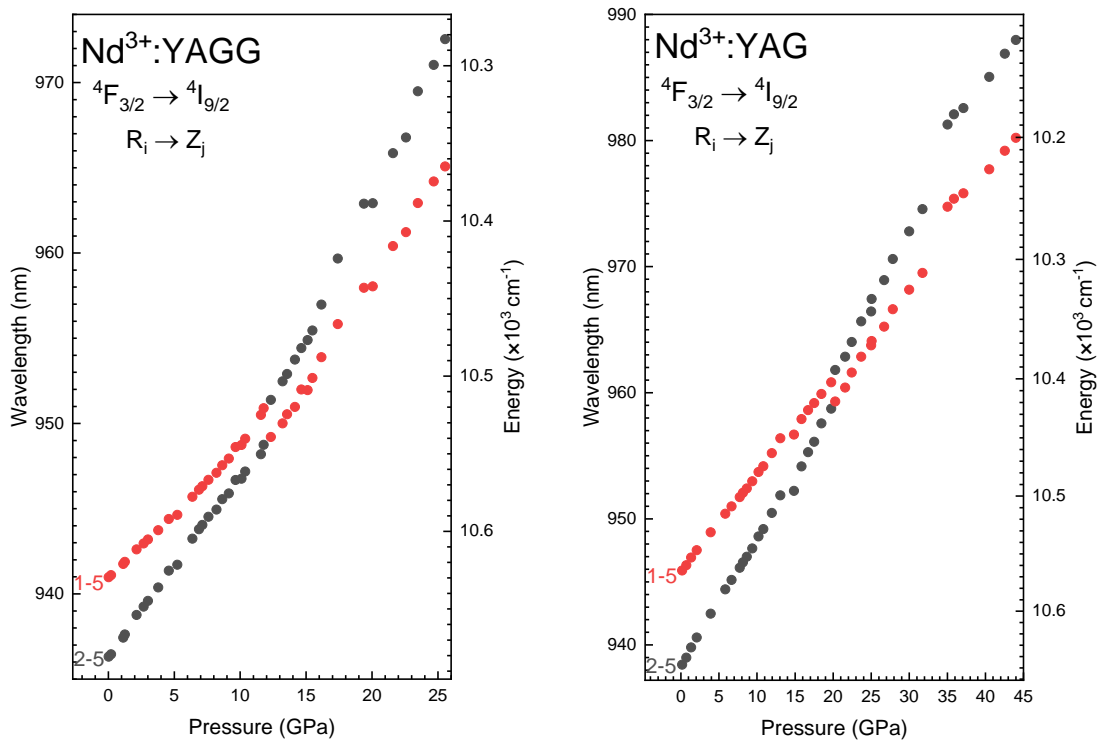

Figure 21. Energy exchanges proposed in pressure study.

According to the temperature and pressure studies, it could be interesting doing an exhaustive analysis for all the peaks behaving, and in the case of the temperature, repeating the same study and adding extreme high ones, and doing a comparative with the other

samples. Besides, it would be really interesting to try to obtain a phase diagram, combining the temperature with the pressure, and a vibrational study using Raman spectroscopy, for ambient and extreme conditions of pressure. It would be appropriate to introduce Nd:YGG measurements and doing a comparative among the three hosts, studying how changes the volume of sites with pressure.

To sum up, previous works made by a research team in the university Carlos III has proposed a crossing of levels $R_{1,2} \rightarrow Z_5$ of the $^4F_{3/2}$ doublet, exchanging their wavefunctions to each other, according to theoretical simulations. In Fig. 21 are proposed the energy exchanges for both samples.

6. Spanish summary

En esta memoria se va a llevar a cabo una caracterización óptica de tres granates dopados al 1 % con iones trivalentes de neodimio Nd^{3+}, cuyas composiciones químicas son $Y_3Al_5O_{12}$, $Y_3Ga_2Al_3O_{12}$ e $Y_3Ga_5O_{12}$, identificándose como Nd:YAG, Nd:YAGG y Nd:YGG respectivamente, tanto en condiciones ambiente como extremas, de temperatura y presión.

En el primer capítulo se presenta una introducción que justifica el interés en utilizar métodos espectroscópicos y la utilidad de los granates en diversos campos. En el desarrollo teórico están introducidos conceptos básicos como la estructura cristalográfica de la red y de la que presentan los iones; así como el formalismo teórico y matemático que posteriormente se utilizará en la sección de Resultados.

En el capítulo de metodología se explican cómo se crecieron los cristales, cómo se prepararon las muestras, y se describen los aparatos utilizados y su configuración para obtener las medidas.

Respecto al capítulo de resultados, se exponen las secciones de condiciones ambiente, la cual está subdividida a su vez en tres subsecciones: la subsección de absorción, en la cual se presentan los espectros de absorción de las distintas muestras identificando las transiciones, sus baricentros, áreas, y líneas de fuerza de oscilador, de dichas transiciones, así como los parámetros de intensidad de Judd-Ofelt obtenidos. En la subsección de luminiscencia, se añaden los espectros de emisión de las muestras, y se adjuntan las líneas de fuerza, sus probabilidades espontáneas de emisión, las tasas de desexcitación y los

tiempos radiativos. Y en la subsección de tiempos de vida, se presentan los tiempos de decaimiento experimentales, y los ajustes a Inokuti-Hirayama, comparándolos mediante el rendimiento cuántico.

Para la sección de condiciones extremas, la subsección de temperatura se tienen diversos resultados provenientes del estudio de las intensidades integradas entre un multiplete termalizado y otro que no lo está, el corrimiento hacia el rojo de un pico con la temperatura y el estudio de las sensibilidades absoluta y relativa, todo ello para la muestra Nd:YAG. Por último, en la subsección de presión, se estudia a presiones extremas el comportamiento de los niveles de energía para las muestras del Nd:YAG y Nd:YAGG, en concreto para los multipletes $R_{1,2} \to Z_5$.

7. References

A

Advatech UK Limited. Datasheet for Nd:YAG. Web link: *https://www.advatech-uk.co.uk/nd_yag.html*

Axe J.D. (1963) *The Journal of Chemistry Physics* No.-**39** Vol.-**5** pp. 1154-1160.

C

Carnall W.T., Fields P.R., Rajnak K. (1968) *The Journal of Chemistry Physics* No.-**8**, Vol.-**10** pp. 4424-4442.

Carnall W. T. (1978) *Energy Level Structure and Transition Probabilities in the Spectra of the Trivalent Lanthanides in LaF₃.* Argonne National Laboratory.

Chiarotti G.L., Ancilotto F., Scandolo S., Tosatti E. (1997) *Science* No.-**275** Issue-**5304** pp. 1288-1290.

Cohen-Tannoudji C., Diu B., Laloë F. (1977) *Quantum Mechanics,* Vol.-II p. 1410.

D

Dong J., Rapaport A., Bass A., Szipocs F., Ueda K. (2005) *Physics status solidi* No.-**13** Vol.-**202** pp. 2565-2573.

Dowell. L.J. (1990) *The Foxter, Dexterand Inokuti-Hirayama Models of the Time Dependence of Fluorescence Amplitude: An Annotated Bibliography.*

J

Judd B.R. (1962) *Physical Review* No.-**3**, Vol.-**127** pp. 750-761.

K

Kamada K., Endo. T., Tsutumi K., Yanagida T., Fujimoto. Y., Hukabori A., Yoshikawa A., Pejchal J. and Nikl M. (2011) *Crystal Growth & Design* No.-**11** pp.-4484-4490.

Kaminskii A.A., Li. L. (1974) *Physics status solidi* No.-**26** pp. 593-598.

Kavaya M. J., Henderson S.W., Magee J.R., Hale C.P., Huffaker R.M. (1989) *Optical Letters* Vol.-**14** pp.776-778.

Krupke W.F. (1971) *IEEE Journal of Quantum Electronics* QE-**7**, No.-**4** pp. 153-159.

L

Latina M.A., Sibayan S.A., Shin D.H., Noecker R.J., Marcellino G. (1998) *Ophthalmology* pp.2082-2090.

Lavín V., Venkatramu V., Monteseguro V., Rathaiah M., Linganna K., Lozano-Gorrín A.D., Hernández-Rodríguez M.A., Martín I.R., Babu P.,Rodríguez-Mendoza U.R., Manjón F.J., Muñoz A., Jayasankar C.K. (2015) *Optical Material Express* No.-**8**, Vol.-**5** pp. 1661-1673.

Lavín V. (2000) *Transferencia de energía entre Iones 4f en vidrios fluorinatos.*

Löhring J., Meisnner A., Hoffmann D., Fix A.,Ehret G., Alpers M. (2011) *Applied Physics B* Vol.-**102** pp. 917-935.

M

Medeiros Neto J.A., Hewak D.W., Tate H. (1995) *Journal of non-Crystalline Solids* Vol.-**103** pp. 201-207.

Morrison C.A. and Leavitt R.P. (1982) *Spectroscopic properties of triply ionized lanthanides in transparent host crystals Handbook of Physics and Chemistry of Rare Earths.*

O

Ofelt G.S. (1962) *The Journal of Chemistry Physics* No.-**3**, Vol.-**37** pp. 511-520

Österberg U., Margulis W. (1986) *Optical Letters* Vol.-**37** pp. 516-518.

R

Recio J.M., Menéndez J.M., Otero de la Roza A. (2016) *An Introduction to High-Pressure Science and Technology* p. 77, 176

Rodríguez-Mendoza U.R., Lalla E.A., Cáceres J.M., Rivera-López F., León-Luis S.F., Lavín V. (2011) *Journal of Luminescence* Vol.-**131** pp. 1239-1248.

Rodríguez-Mendoza U.R., León-Luis S.F., Muñoz-Santiuste J.E., Jaque D., Lavín V. (2013) *Journal of Applied Physics* Vol.-**113** No.-**213517** pp. 1-8

S

Strohmaiera S.G.P., Eichlera H.J., Czeranowskyb C., Ilerib B., Petermannb K., Huberb G. (2007) *Optics Communications* Vol.-**275** pp. 170-172.

W

Walsh B.M., Barnes N.P., Hetcheson R.L., Equall R.W., Di Bartolo B. (1999) *IEEE Category No.99CH3701*

Walsh B.M. (2006) *Advances in Spectroscopy for Lasers and Sensors* pp. 403-433.

Y

Yumashev K.V., Loiko P.A., Vilejshikova E.V., Khaidukov N.M., Méndez-Ramos J., Mateos X. (2017) *Journal of Luminiscence* Vol.-**190** No.-**131** pp. 37-44.

8. Appendix: programs

It can be consulted the programs which were made to obtain the Judd-Ofelt calculations, clicking in the chart: *Google Drive link*